SANDIA REPORT
SAND2007-7680
Unlimited Release
Printed Month and Year

Large-Area Metallic Photonic Lattices for Military Applications

Ting S. Luk

Prepared by
Sandia National Laboratories
Albuquerque, New Mexico 87185 and Livermore, California 94550

Sandia is a multiprogram laboratory operated by Sandia Corporation,
a Lockheed Martin Company, for the United States Department of Energy's
National Nuclear Security Administration under Contract DE-AC04-94AL85000.

Issued by Sandia National Laboratories, operated for the United States Department of Energy by Sandia Corporation.

Available to DOE and DOE contractors from
U.S. Department of Energy
Office of Scientific and Technical Information
P.O. Box 62
Oak Ridge, TN 37831

Telephone: (865) 576-8401
Facsimile: (865) 576-5728
E-Mail: reports@adonis.osti.gov
Online ordering: http://www.osti.gov/bridge

Available to the public from
U.S. Department of Commerce
National Technical Information Service
5285 Port Royal Rd.
Springfield, VA 22161

Telephone: (800) 553-6847
Facsimile: (703) 605-6900
E-Mail: orders@ntis.fedworld.gov
Online order: http://www.ntis.gov/help/ordermethods.asp?loc=7-4-0#online

SAND2007-7680
Unlimited Release
Printed Month Year

Large-Area Metallic Photonic Lattices for Military Applications

Ting S. Luk
Photonic Microsystems Technology
Sandia National Laboratories
P.O. Box 5800
Albuquerque, New Mexico 87185-MS1082

Abstract

In this project we developed photonic crystal modeling capability and fabrication technology that is scaleable to large area. An intelligent optimization code was developed to find the optimal structure for the desired spectral response. In terms of fabrication, an exhaustive survey of fabrication techniques that would meet the large area requirement was reduced to Deep X-ray Lithography (DXRL) and nano-imprint. Using DXRL, we fabricated a gold logpile photonic crystal in the <100> plane. For the nano-imprint technique, we fabricated a cubic array of gold squares. These two examples also represent two classes of metallic photonic crystal topologies, the connected network and cermet arrangement.

ACKNOWLEDGMENTS

The successful completion of this project is the result of the efforts of many people. Ganesh Subramania, John Williams, and Bill Sweatt, explored various viable fabrication technologies. Ihab El-Kady and David Peters performed the Sandia modeling work. Fabrication was performed by John D. Williams, Ganesh Subramania, Carrie Schmidt, Stan Kravitz at Sandia National Laboratories. Rick Mccormick managed the project.

Table of Content

1. Introduction

Photonic crystals have been a topic of intense research over the last 10 years, and photonic crystal-based applications are starting to reach maturity in fields such as bio sensing and fiber optics. For many military platforms large areas covered with photonic crystal would be advantageous to control the platforms' optical and thermal characteristics. For example, photonic bandgap (PBG) materials are poised to have enormous impact on the thermal management of a variety of military platforms, and on the creation of revolutionary optical emission technologies (e.g. displays for infrared scene generation). This project leverages Sandia expertise in PBG design/modeling to optimize the PBG structures for utilization of new materials, and efforts in nanoimprinting and metal deposition/plating processes to rapidly fabricate large sheets of new PBG designs. The new materials and form of these PBG structures will broaden the scope of applications.

Photonic crystals can be thought of as the photonic analogues of semiconductors. When correctly designed, these engineered photonics structures can exhibit a photonic bandgap: a range of photonic energies which are forbidden to exist in this structure. Another way of considering this is that the density of allowed states of photons with energies within the bandgap goes to zero. It is also possible to increase the density of states to engineer the absorption of the crystals. Photonic bandgaps have been measured in 1-D (similar to Bragg gratings), 2-D (a planar "slice" crystal), and 3-D synthetic crystals. For many applications full 3-D photonic crystals are desirable for their ability to "mold light" across a wide range of wavelengths and angles. However, current PBG fabrication techniques offer limited materials choices (tungsten, aluminum and silicon) and small areas: square inch rather than the square meter areas needed in these applications.

In order to enhance mechanical strength, photonic crystals with filler material are considered. In general, the effects of the filler (the low dielectric background in which the metallic entities are embedded) are limited to any bulk absorption characteristics that it may posses. This in turn implies that its effects will reducing transmission and reflection signatures of the photonic lattice, and will have negligible effects on the gap size or location. Thus, for the case of a metallic photonic lattice, where the photonic gap becomes quite strong by stacking only a few unit cells, the incoming electromagnetic wave penetration is limited to only a few surface layers in the photonic gap frequency regime, and hence the result of a filler absorption should be to reduce the reflectivity of the photonic lattice from near perfect (100%) by a few percentiles (say to ~%90). On the other hand, in the transmission regime of the photonic lattice, where Bloch modes are allowed to propagate, the transmission of lattice will be reduced by a factor proportional to the effective optical path length within the photonic lattice. However, this effective optical path length within the photonic lattice can be far larger than the simple geometrical length because the group velocities of the wavelengths at various band edges are much slower. Reduced group velocity (slow light) increases the interaction time and hence the effective absorption cross-section of the lattice.

A general survey and theoretical understanding of the design forms and materials for large area PBGs was undertaken. Next, the manufacturability and tolerance analysis of the

specific forms were studied and selected as vehicles for our fabrication experiments. Photonic band gap formation can be understood as a "synergic interplay" between the microscopic scattering resonance from the dielectric material contained in a single unit cell of the photonic crystal and the macroscopic resonance dictated by the geometrical arrangement of the repeating unit cells of the dielectric microstructure. A photonic band gap is facilitated only if the geometrical parameters of the crystal are such that both the microscopic and macroscopic resonances occur at precisely the same wave length and both of these scattering mechanisms are independently strong. Because the photonic band gap manifests itself as a band in cermet topologies (disconnected scattering centers) and as a cutoff in network topologies (connected scattering centers), the general rule of thumb is that network topologies will express more resilience to fabrication errors as there is only one fundamental band edge to deal with versus two in the case of cermet topologies. We have created design matrices for relevant photonic structures shown in Table 1.1, identifying ”global” designs based on topology and symmetry of the high dielectric material, as well as for specific photonic crystal design tradeoffs. The relative ranking (1=best, 3=worst) is a “snapshot” of our present theoretical understanding. Based on these considerations, we chose to focus on the cubic array of cubes (COAC) and tilted logpile structures. The COAC is attractive because it requires only two layers to make up a unit cell. This reduces number of steps in the fabrication process substantially.

Design	**Scalabiliy**	**Fab. Tolerance sensitivity**	**Manufactur ability**
Cermet cubic topology	Limited only by fab.	3	2
Network cubic topology	Limited only by fab.	2	1
Diamond cermet topology	Limited only by fab.	2	3
Diamond network topology	Limited only by fab.	1	2
Face centered tetragonal network topology	Limited only by fab.	2	1
Cubic array of cubes	Limited only fab. (minimum feature size and aspect ratio).	3	2
Logpile	Limited only fab. (minimum feature size and aspect ratio).	1	1
Tilted logpile	Limited by LIGA mask	1	1
Holographic diamond structure	Limited by infiltration capability and uniformity of the film	3	3
Twisted rod (spiral) structure	Limited by glancing angle deposition, repeatibility and accuracy	2	3

Table 1.1: Design matrices for PBG structures. The ranking 1 is the best and 3 is the worst.

In this report, we will describe two approaches of photonic crystal fabrication that are scaleable to large area [1]. A first method is deep X-ray lithography (DXRL) to create a mold in PMMA which is then filled by electro-deposition of gold, copper, or other materials. A second approach uses nano-imprinting to define the mold, which is filled using evaporative deposition or atomic layer deposition of metals or other materials.

We also developed modeling tools to optimize the design of the photonic crystal and for fabrication tolerance analysis. In addition, we have developed conceptual fabrication techniques for more exotic spiral structure and chiral photonic crystals.

2. Fabrication, modeling and testing of tilted logpile structure

2.1 Background

In the late 1990's Iowa State researchers [1] developed a model design for producing a wider 3-D band gap using a logpile (or woodpile [2]) design. The Iowa State structure was first realized by Lin and Fleming [3] at Sandia National Laboratories using traditional lithographic patterning techniques and building it layer by layer. The first structure had a band gap between 8 and 14 μm. Since its original publication, this structure as been repeated by numerous researchers for bands in both the IR and visible using metals, ceramics, and polymers, in both the direct and the inverse structural patterns. However, many of these lattices are comprised of materials that do not provide a large enough optical index contrast within the crystal to eliminate all transmission in the photonic band. While most metals demonstrate sufficient contrast between 400 and 800 nm, most polymers do not. Metals like gold, tungsten, and silicon have sufficiently high indices to prevent nearly all transmission in the range of the photonic band gap. Woodpiles using both silicon and tungsten have been demonstrated by Lin and Fleming. Both Si, and W have high melting points, making them ideal materials for TPV applications. Although gold does not have a high melting point, it has excellent optical properties in the IR spectrum and is easily electrodeposited into high aspect ratio features. The problem with the woodpile structure is that it requires multiple aligned lithographic patterning steps. This drives up both the cost and processing tolerances for producing such a structure. In addition, this fabrication technique is incompatible with flexible substrate. An alternative approach is LIGA(DXRL) which allows fabrication of this structure with different crystal plane on the substrate (tilted logpile).

The LIGA process was developed at the IMT (then Institute for Nuclear Engineering), in the early eighties under the leadership of Prof. Dr. E.W. Becker and Dr. W. Ehrfeld. LIGA is an acronym standing for the main steps of the process, i.e., deep X-ray lithography, electroforming, and plastic molding. These three steps make it possible to mass-produce microcomponents with high aspect ratio at a low-cost. The LIGA technique uses X-rays generated by synchrotron light source to pattern thick photoresist on a metallize substrate. X-rays emitted from the light source are highly collimated and capable of patterning photoresist such as PMMA with critical dimensions of much less than 1 um and aspect ratios significantly greater than 10:1. The patterned structure is then developed in a liquid solvent to remove low molecular weight polymeric materials leaving the material defined by X-ray exposure. The last step in the LIGA process involves the subsequent molding of electroplated parts in plastic with the intent of replicating several plastic molds for a single electroplated master.

Toader and John's process scheme [4] requires the use of either Deep X-ray lithography (DXRL) or interference lithography to generate the high aspect ratio patterns required to pattern a structure 2-3 lattice spacings deep into photoresist. However, the improvement of interference lithography techniques using high aspect ratio resist such as SU-8 have allowed for the production of plastic tilted logpile patterns over areas of a few hundred square microns. [5].

While this technique has the potential to produce large area photonic lattices, it has yet to be demonstrated. Alternatively, DXRL is a mature technique for the generation of high aspect ratio lithographic patterns over areas of a few square inches. Unfortunately, hardware requirements for submicron translation and alignment of a DXRL mask to a substrate have prevented the production of this device.

2.2 Fabrication

We developed a new DXRL approach that eliminates the need for alignment altogether. Instead of exposing one orientation of the structure and shifting the mask by approximately 1.5 um prior to exposing the second, the new method clamps the mask and substrate together prior to exposure and completes a set of different tilt and rotation angles to expose the pattern. The first exposure requires rotating the mask and substrate by an 8 degree angle with respect to the incident beam. The mask and substrate are then tilted at a 45 degree angle toward the incident X-ray beam and exposed. After the first exposure, both mask and substrate are rotated together

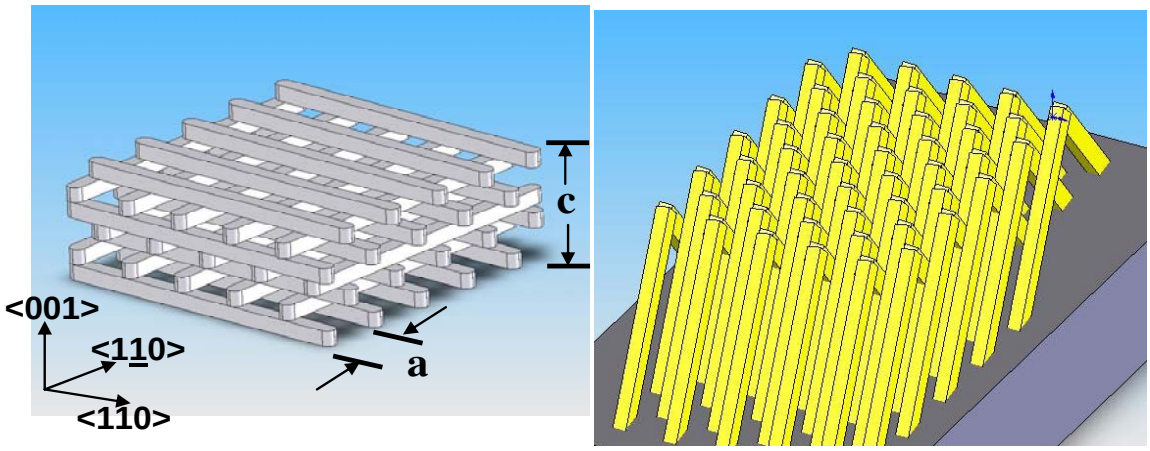

Figure 2.1: Designation of crystal orientation of logpile structure: the left panel is the conventional logpile structure fabricated with a layer-by-layer lithrography approach, b) the right panel shows the orientation of the tilted logpile structure built on a substrate using LIGA.

by 180 degrees and exposed to produce the opposite pattern. This second rotation is equivalent to tilting the mask/substrate fixture 45 degrees away (or at a negative angle) with respect to the incident beam. This approach can be performed with commercially available DXRL scanner technology and does not require fine alignment of the mask and substrate.

This technique offers a unique method for fabricating 3-dimensional photonic lattices based on the Iowa State "logpile" structure with <100> plane on the surface of the substrate instead of the conventional <001> (see Figure 2.1). The tilted logpile has the same lattice structure as the conventional woodpile PBG. It is simply rotated with respect to the substrate by 90 degrees out of plane and 45 degrees in-plane to orient the <110> direction normal to the substrate. The novelty to this approach is the single step process that does not require any critical sub-micron alignment.

The DXRL mask shown in Figure 2.2 was fabricated by electroplating 0.75 μm of gold onto a 1 μm thick silicon nitride membrane. Sufficient contrast is achieved with a 0.4 μm thick

gold pattern for exposures normal to the incidence beam. Exposure with Deep X-ray lithography using the 1.3 GeV synchrotron light source at the Center for Advanced Microstructures and Devices was performed at Louisiana State University. The use of a 'white light" source with no mirror provides a 1-10 KeV photon spectrum. Higher energy X-rays from this spectrum produce a 1-2 μm wide secondary exposure at the foot of the pattern. In this case, high energy photons would have exposed the entire bottom surface of the resist leading to a delamination of the pattern during development. Therefore, the X-ray beam was filtered using an 89^o incidence mirror to provide a soft X-ray spectrum of 0.5 to 2 KeV photons. [6]. The filtered spectrum reduced secondary exposure, allowing 1 um features to be patterned into 20 μm of PMMA. Line broadening can be further reduced by depositing a thicker gold absorber on the nitride membrane. Typical feature size this technique can achieve is about 1 μm.

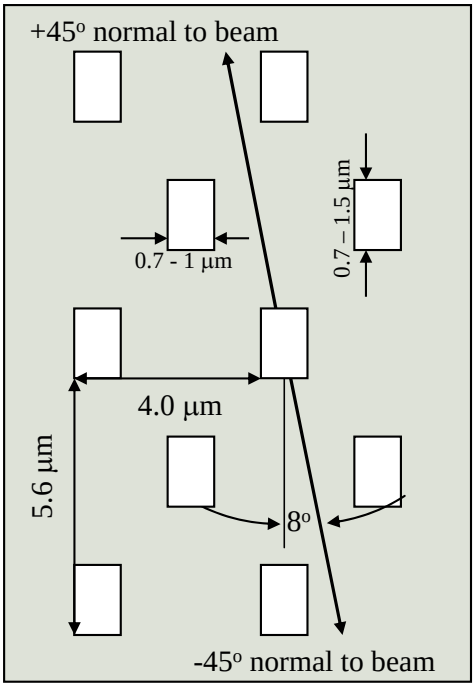

Figure 2.2: Mask pattern for the LIGA tilted logpile fabrication.

The logpile was patterned using two exposures. For each exposure, the x-ray beam with 48x3mm sweeping through a length of 100mm of the substrate. An exposure time 4-17 hrs is required to expose a 4" wafer. The mask and substrate remained clamped with 25 μm spacing between them for both exposures. The first exposure was performed with the mask and substrate oriented at a 45^o incidence angle to the X-ray beam and rotated perpendicular to the incidence angle by 8 degrees. The second occurred immediately after by simply rotating the mask and substrate perpendicular to the incidence angle by an additional 180 degrees. This effectively changed the angle of incidence for the exposure from +45^o to -45^o, thereby patterning lines perpendicular to those exposed in the first exposure, as shown in Figure 2.1. The resulting pattern is a series of exposed crosshatched planes entering the PMMA film at a 45 degree angle. The planes have a width of 0.9 um and are shifted by ½ a lattice period with respect to one another.

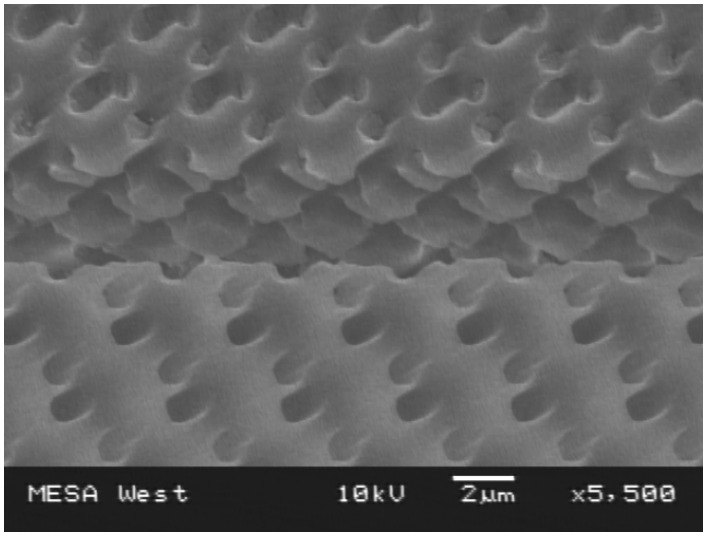

Figure 2.3: SEM of a developed PMMA pattern. The resist is cracked along the pattern showing the side profile of the crosshatched lines that will be plated to produce a tilted logpile.

After exposure, the substrates were returned to Sandia National Laboratories where the remainder of the processing is performed. Exposed PMMA was developed in GG developer using gravity assisted mixing. After development, the sample is rinsed in GG rinse and water prior to removal of the titanium film used to promote adhesion of the PMMA film on the substrate. An example of the developed PMMA structure is presented in Figure 2.3. The sample used in this figure was removed from the rinse bath and dried without plating. Stress in the PMMA film caused large cracks in the resist that provide an excellent view of the sidewall profile. The resist profile within the PMMA is clearly presented as crosshatched lines moving from left to right, and right to left in the middle of the SEM. Another pattern that becomes clear in this figure is the dual exposure present on the top surface of the resist. The light and dark holes depicted show each of the slanted holes patterned during the lithography process. This structure is clearly shown in the sidewall of the resist pattern. The doublet effect is due to both the proximity gap between the mask and the resist surface, and small changes in thickness present from the spin casting the resist. Aside from aesthetics this effect has little effect on the overall performance of the pattern. The resist is simply a mold for the electroplate metal that will be plated to a uniform thickness over the entire pattern.

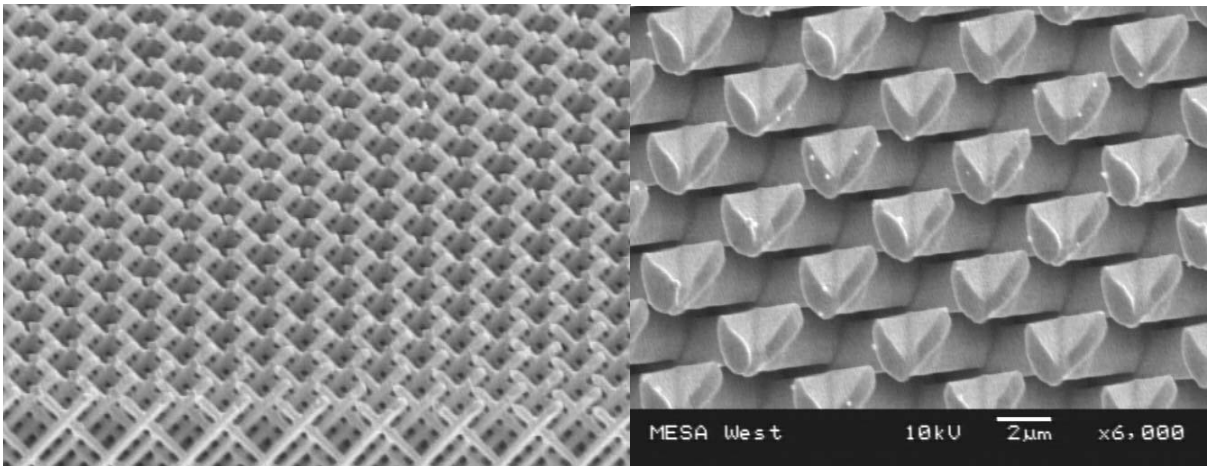

Figure 2.4: SEMS of a tilted logpile comprised of 2.2 x 0.8 μm^2 bars at a 4 μm pitch (left) 50 μm field (right) 20 μm field top view showing small gaps between rows of connected columns.

After the titanium etch, samples were placed directly into a gold electroplating bath without drying. Gold was deposited into the developed pattern at a rate of 0.2 μm /min until the desired thickness was obtained. The resist was then stripped to reveal a gold logpile with an air dielectric tilted with <110> direction normal to the plane of the substrate.

Figure 2.4 shows an SEM of the electroplated tilted logpile after the resist is stripped. The electroplated gold structure was plated was 13 μm tall to produce 2.5 unit cells of photonic crystal in the vertical direction. The thinnest beams plated were 0.8 μm wide and 2 μm thick with an aspect ratio of about 15:1. The photonic crystal presented in Figure 2.2 has beam widths of 1 μm and thicknesses of 2.5 μm. The size of the crystal in Figure 2.4 is 5 x 5 mm^2. The few defects present were primarily particles on the substrate during the photoresist spin-casting process. These can be overcome by implementing cleaner procedures during resist processing. It

is believed that these structures can be produced over the entire width of an X-ray mask spanning at least 1.5 in^2. This fabrication technique has resulted in a patent.

2.3 Characterization

Samples were characterized with a hemispherical directional reflectometer (HDR) to determine the total, diffuse, and specular reflectivity of the material. The HDR uses a reciprocal process to measure the total light reflected by a material from a source at a given incident angle of 19 deg. Figure 2.5 shows the total reflected light from four different photonic crystals. Two of the PBGs tested had the rod cross sections of 2.2 x 1 m^2. These structures are fully dense, meaning there are no gaps between sets of cross beams when looking directly down on the lattice. The other two structures have small spaces between layers of the PBG. Figure 2.4 clearly shows these gaps between rows of connected columns in the fabricated tilted logpile. As the column width decreases, a transmission window opens in the photonic band gap. The shape and location of this dip varies but is roughly centered between 8 and 12 microns.

The emission peak typically present at wavelengths just below the band gap is observed as a relatively sharp dip in the total reflection data presented. Measurements were taken using the assumption that the samples themselves were totally opaque at the wavelengths of interest and showed no IR transmission, because the photonic structure is plated in gold on a thin gold film. Therefore, approximate emission curves can be generated by subtracting the total reflectivity of the sample from unity. E=1-R-T, where reflectivity is the measured total reflectivity and transmission is zero.

Blocking the specular signal in the HDR, allows for the measurement of diffuse reflectance. The specular component is then calculated by subtracting the diffuse from the total (Specular = Total - Diffuse). Since these samples are small, great care was taken to align the system to the samples with a 2.5 mm aperture that allowed for the collection of angular data up to 60-degree incidence. The azimuthal angle is zero and is measured with respect to the plane defined by the double exposure. Total and specular reflection is presented in Figure 2.7 for a fully dense tilted logpile PBG at different angles of incident light. For these measurements light is shown parallel to the 5.6 m (or long) axis of the tilted logpile pattern. Data from light in the perpendicular direction also demonstrates photonic lattice behavior along a different axis of the 3-D Bravais lattice.

Theoretical computation of this structure turns out to be non-trivial using the transfer matrix methodology because the pattern parallel to the surface is changing continuously which requires extremely large number of step to go through one period.

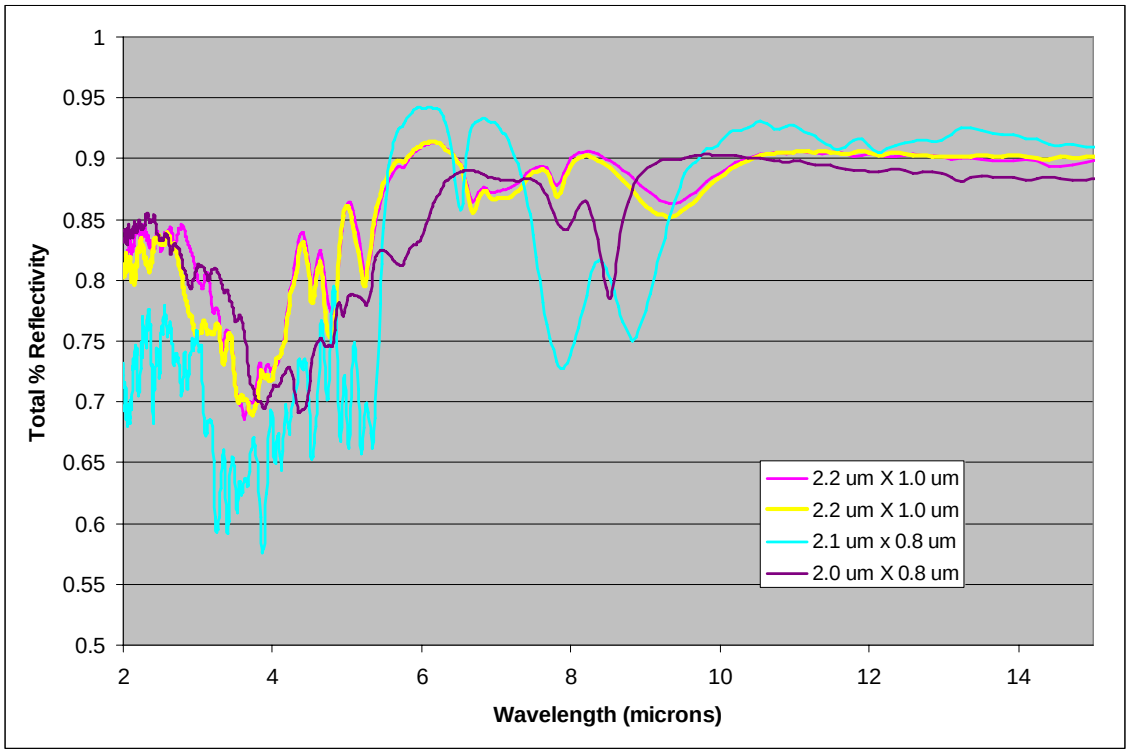

Figure 2.6: Total reflectivity data for 4 different titled logpile PBG structures with different beam cross sections showing band gaps between 5 and 15 microns

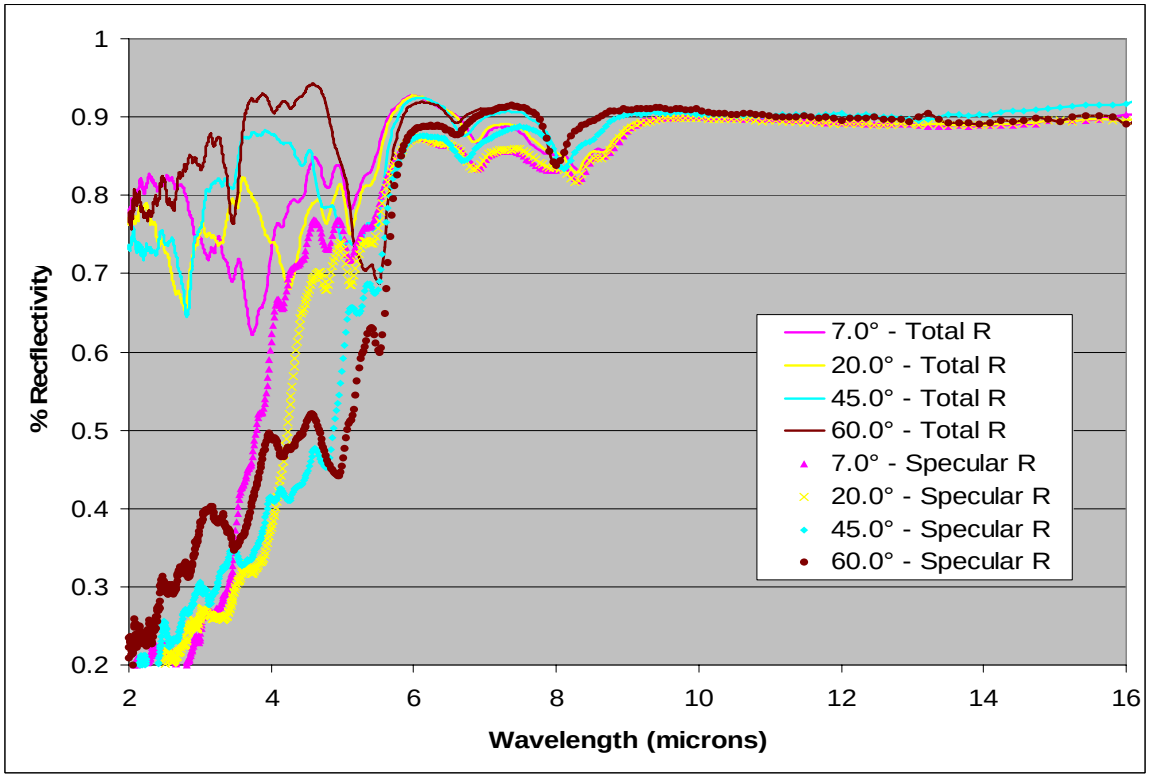

Figure 2.7: Total and Specular reflectivity data for a tilted logpile with beam cross sections of 2.2 x 1 μm^2. Measurements are taken for incident angles between 7° and 60°. Incident light is shown parallel to the long axis of the lattice structure.

2.4 References

[1] Ho, K. et al., Photonic band gaps in three dimensions: new layer by layer periodic structures, Solid State Comm. 89, 413-416 (1994).
[2] H.S. Sozuer, and J.P. Dowling, Photonic calculations for woodpile structures, J. Modern Optics 41, 231-239 (1994).
[3] S.-Y. Lin, and J.G. Fleming, Photonic band-gap microcavities in three dimensions, Physical Rev. B 59, 579-582 (1999).
[4] O. Toader, M. Berciu, and S. John, Photonic band gaps based on tetragonal lattices of slanted pores, Phys. Rev. Lett. 90(23), 233901 (2003).
[5] M. Deubel, M. Wegener, A. Kaso, and S. John, Direct laser writing and characterization of slanted pore photonic crystals, Appl. Phys. Lett. 85(11), 1895-1897, (2004).
[6] C. Cuisin, et al., Sub-micrometre dielectric and metallic Yablonovite structures fabricated from resist templates, Opt. Quant. Elec. 34, 13-26 (2002).

3. Fabrication, modeling and testing of COAC structure

3.1 Background

Nano imprint lithography (NIL) was developed by Prof. Stephen Chou of Princeton University [1,2]. NIL allows for rapid, top-down nanopatterning of large areas using a hard "master" mold fabricated using conventional mask writing techniques such as electron beam lithography [3]. Two main variants of nanoimprint lithography are thermal (T-NIL) and photocurable (P-NIL) NIL. A picture of a thermosetting Nanonex nanoimprint system is shown in Figure 3.1a. In the T-NIL approach a thermosetting polymer is first spun cast on a wafer followed by imprint of the mold containing the desired pattern (Figure 3.1b). The polymer is baked to the thermosetting temperature to set the imprint pattern. The mold is released and the pattern on the polymer is then transferred to the underlying substrate through reactive ion etch process. The T-NIL approach has the advantage of using opaque imprint molds but is slower

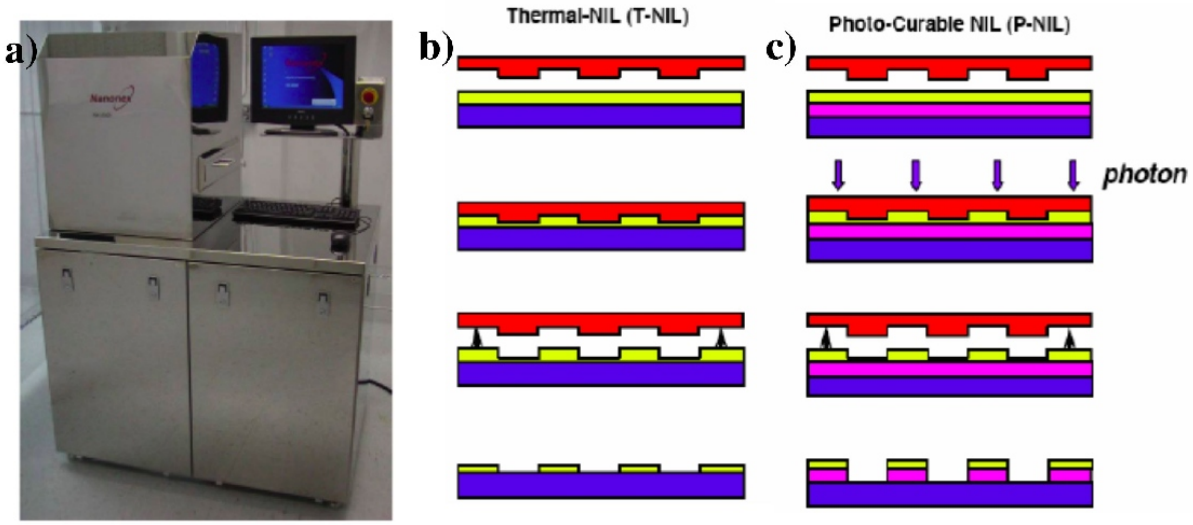

Figure 3.1 a) Nanonex thermal nanoimprint system b) Schematic of a thermal nanoimprint approach c) Schematic of a UV nanoimprint system.

because of the time needed for thermosetting. The P-NIL approach instead uses a UV curable polymer and the pattern is set into the polymer by exposing it to UV light through a transparent mold (Figure 3.1c). This approach is advantageous for multilevel structures when alignment is a requirement as a smaller sized NIL imprint dye size can be utilized in a step and repeat fashion. The NIL approach has several advantages over conventional photolithography and is a potentially inexpensive approach that can be scaled to large areas. The main features that make nanoimprinting attractive for large scale manufacturing are 1) high throughput with a potential resolution limit of ~ 6nm 2) there are no issues with mixing small and large features on the same mask 3) the method is self-planarizing making it attractive for multilayer fabrication 4) resolution is relatively independent of print area 5) can be printed on curved surfaces. The last feature is important as it lends to the possibility of "roll-to-roll" imprint for scaleable fabrication [4].

3.2 Fabrication of "Cubic array of Cube" (COAC) structure

As mentioned in the introduction, the COAC photonic band gap crystal based on gold scatterers (cubes) was chosen as an example structure primarily due to relative ease of fabrication despite its low tolerance for fabrication errors. One needs only 3 layers to fabricate two unit cells along the stacking direction to observe strong photonic band gap effect.

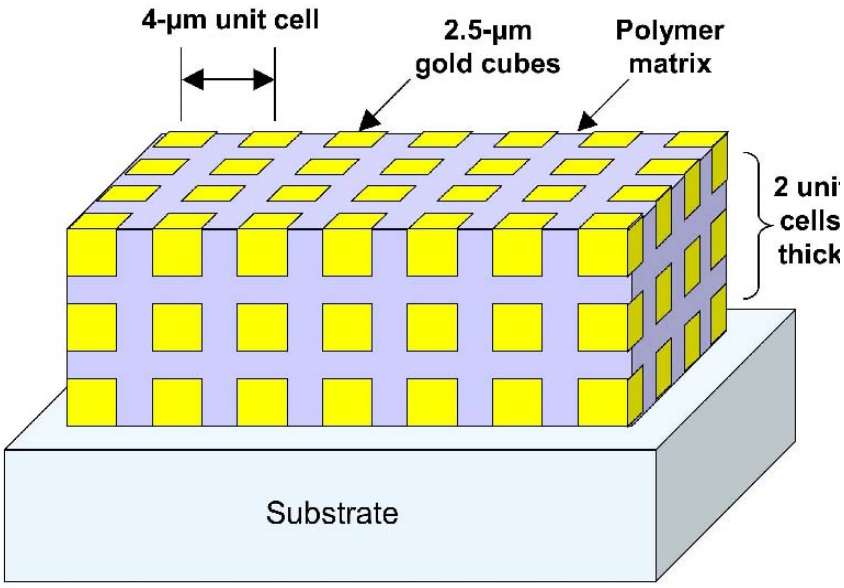

Figure 3.2: Schematic of 2 unit cells of cubic array of gold cube (COAC) structure with 2.5 μm cubes placed at the corners of a 4 μm cube

The cermet topology of this structure allows for the choice of the low refractive index (n ~ 1.5) matrix material to be a flexible polymer (e.g., polyethylene) potentially allowing for roll-to-roll processing leading to large area free standing PBG. As a proof of concept demonstration we chose to fabricate this structure to have a bandgap in the mid-IR range for thermal applications. Computer simulations based on rigorous coupled wave analysis (RCWA) predict that the cubic array of gold cubes of dimensions (2.5 μm X 2.5 μm X 2.5 μm) arranged in the corner of a cube of dimensions (4 μm X 4 μm X 4 μm) in a low index matrix of n ~ 1.5 (Figure 3.2) gives rise to two bands one between ~5-9 μm and another between ~11-20 μm (Figure 3.3a). The short wavelength band shows considerable movement upon change of incidence angle from 0 – 45 degrees (Figure 3.3b) while the long wavelength gap show less movement indicating better

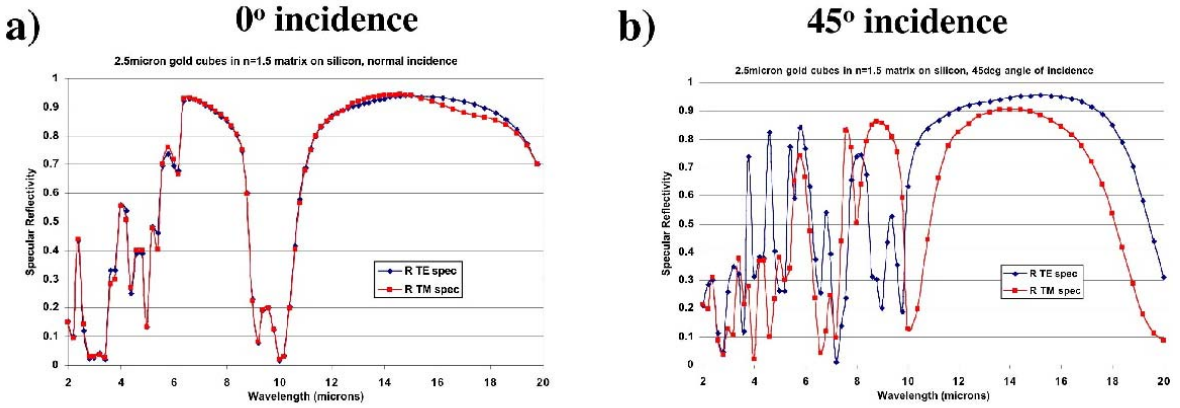

Figure 3.3 a) RCWA simulation of the specular reflectance structure described in figure 2 at normal incidence. b) Simulations at 45 degree incidence angle.

overlap of bands along different Brillouin zone directions. The structural dimensions are large enough to enable feature alignment between different layers during fabrication using contact lithography tools. We considered several candidate materials for the low index matrix (e.g., BCB, polyethylene, polystyrene, zeonor etc.) and chose polyethylene as the best candidate. Polyethylene has a reasonable refractive index (n 1.5) and relatively good transmission in the thermal IR. It has sharp resonances at wavelengths of ~ 3.4 μm, 6.9 μm and 13.9 μm (Figure 3.4a) [5]. However, it is a relatively challenging material to process as it dissolves sparingly in most solvents and hence is difficult to spin into thick layers. Therefore, to enable process development during the initial stages we considered BCB despite its poorer absorption properties showing broad absorption lines between 6-15 μm (Figure 3.4b) and because its processing conditions were well understood.

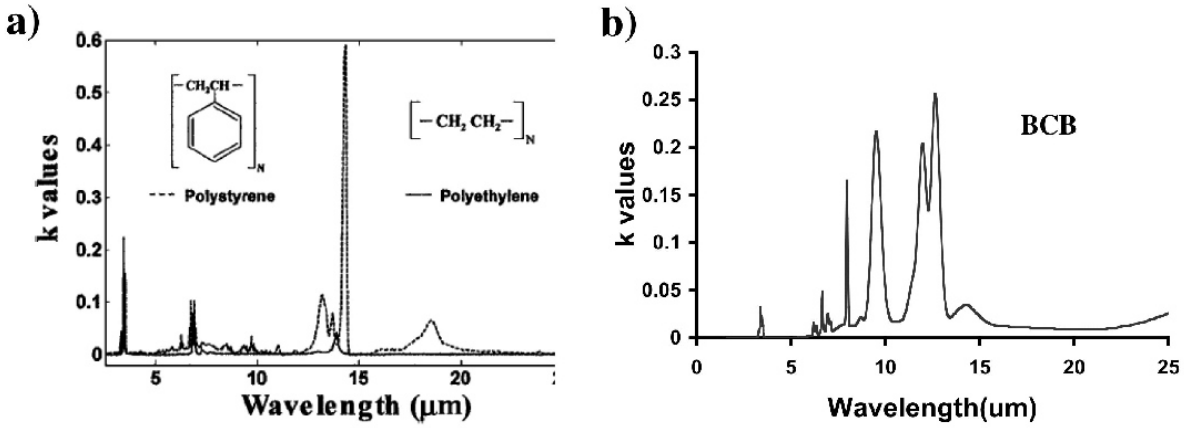

Figure 3.4: a) Imaginary part of the refractive index (k) of polystyrene and polyethylene (PE) . PE has fewer (3) and sharper absorption lines with a smaller values than PE. b) Imaginary part of refractive index for BCB. The peak values are considerably larger and wider than that for PE.

The first set of structures was fabricated using a combination of wet chemistry and electroplating to deposit the 2.5 μm thick gold layer. We started with the evaporation of a thin

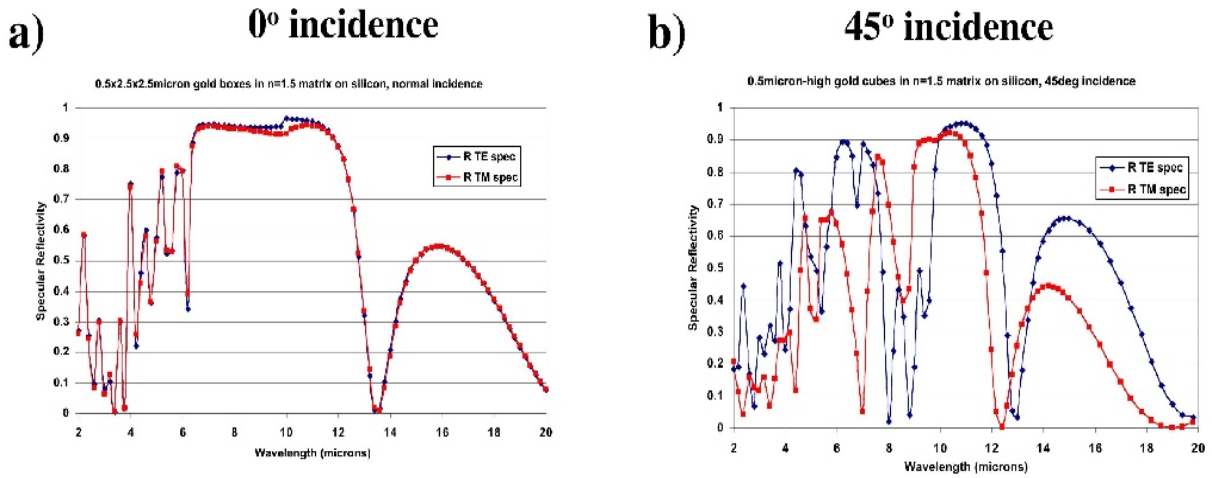

Figure 3.5: RCWA simulations for modified COAC structure with 0.5 micron thick gold instead of 2.5 micron as in the ideal case. a) Normal incidence reflectance measurement b) 45 degree incidence.

Ti/Au layer on the substrate as a seed layer for electroplating. Photoresist was spun onto the seed layer, patterned, and then transformed into a mold using standard photolithography chemistry. Cubes were gold plated into the resist pattern prior to stripping the photoresist using either acetone or oxygen plasma. Both processes resulted in delamination of the underlying polymer film required to fill the matrix. Further investigations lead us to believe that the film under the resist layer was absorbing the plating solution and delaminating from the substrate. As a second approach we attempted a metal liftoff processes using evaporated Ti/Au and a developer soak that did not aggressively attack BCB or polyethylene films beneath the resist. However, the relatively long evaporation time (~ 40 min) needed to deposit 2.5 μm thick layer of gold resulted in the overheating of the resist layer causing it to flow and deform the structure in addition to bubbling of the polymer matrix layer. This resulted in the production of large defects

in the lattice and thereby making alignment of the next layer impossible. The above experiments directed us towards the following important requirements: 1) a dry process involving minimal amounts of solvent processing 2) thinnest layer of gold needed to observe photonic band gap effects so as to conserve precious metal usage as well as optimize deposition time 3) increase source to substrate distance during evaporation. We performed RCWA modeling of the structure by reducing the thickness of gold to 0.5 μm and found that we still obtained a broad reflectance band between 6-12 μm wavelength (Figure 3.5a) at normal incidence but it is reduced to ~9.5-12 μm at 45 (Figure 3.5b) degree incidence angle.

We also developed a new dry processing method for the fabrication (Figure 3.6). First a gold layer is evaporatively deposited on the previously completed layers (or on the bare substrate).

1. A thermal imprint resist is spun on the gold layer.

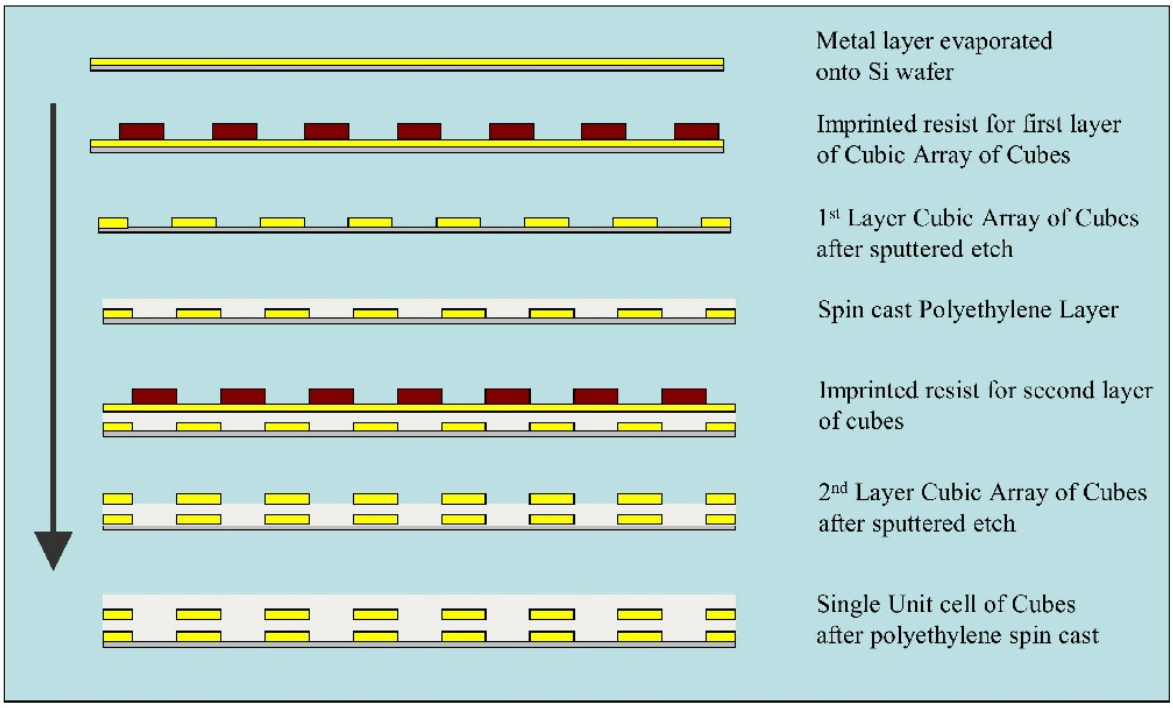

Figure 3.6: Schematic of the "dry" approach to fabrication of COAC structure with Au.

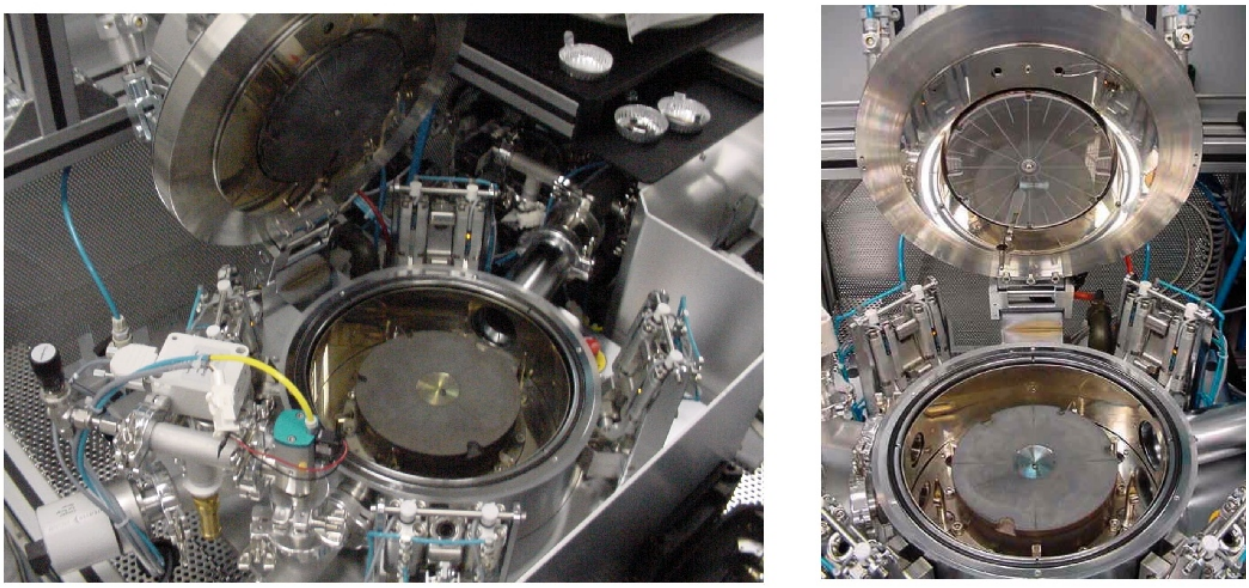

Figure 3.7: Electronic Vision wafer bonder system used as the nanoimprint system

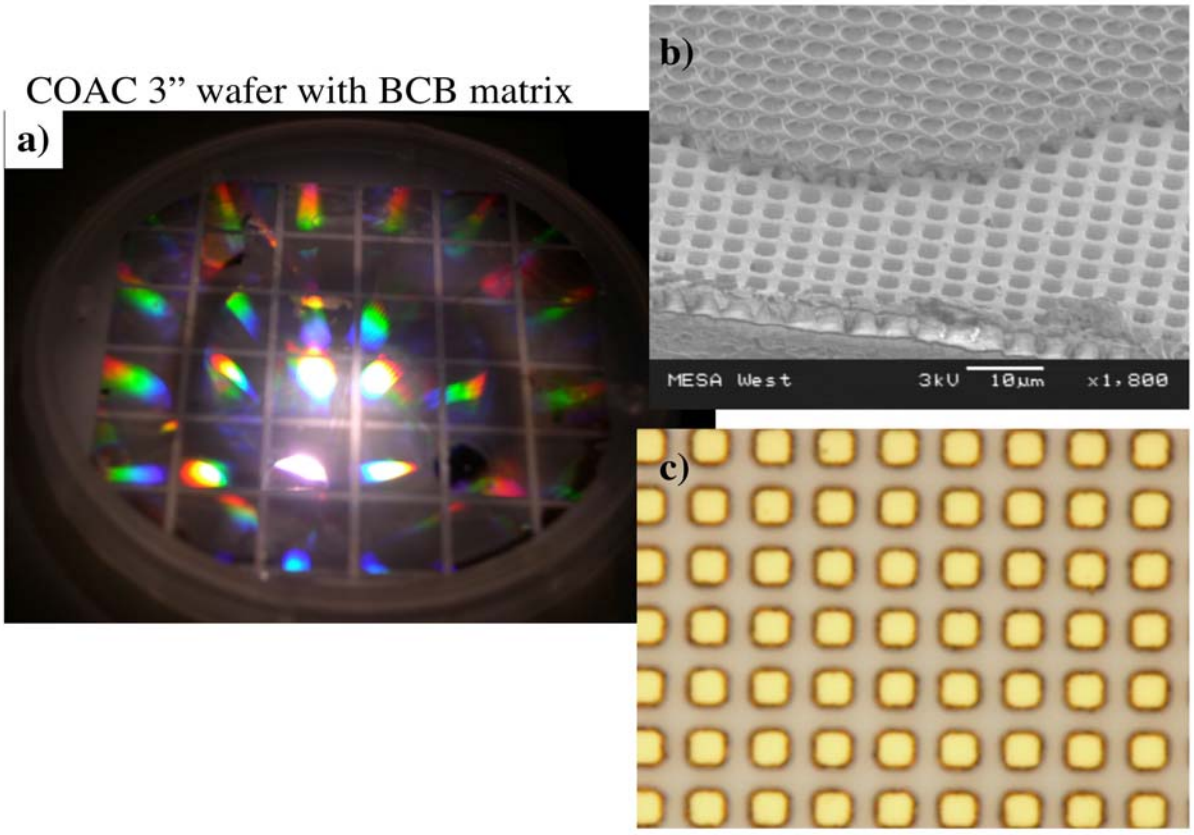

Figure 3.8: a) COAC structure on 3” wafer b) Perspective SEM view of structure c) Top view optical image.

2. A master mold is fabricated on a 4” silicon wafer by patterning it with the optical mask using contact photolithography followed by reactive ion etching.

3. The pattern on the silicon master mold is then imprinted on to the thermal resist using Electronic Vision 520 wafer bonder (Figure 3.7).
4. After the removal of the residual layer reactive sputtering consisting of energetic Ar ions removes the gold away from the imprinted region.
5. The excess imprint resist is stripped off by oxygen plasma leaving behind an array of Au cuboids.
6. Next a ~ 1.5 micron thick PE layer is spun on and dried overnight to harden.
7. The sample is then ready for the deposition of gold for the next layer and steps 1-8 are repeated for additional layers.

Figure 3.8 shows a COAC in a BCB matrix fabricated on a 3" Si wafer.

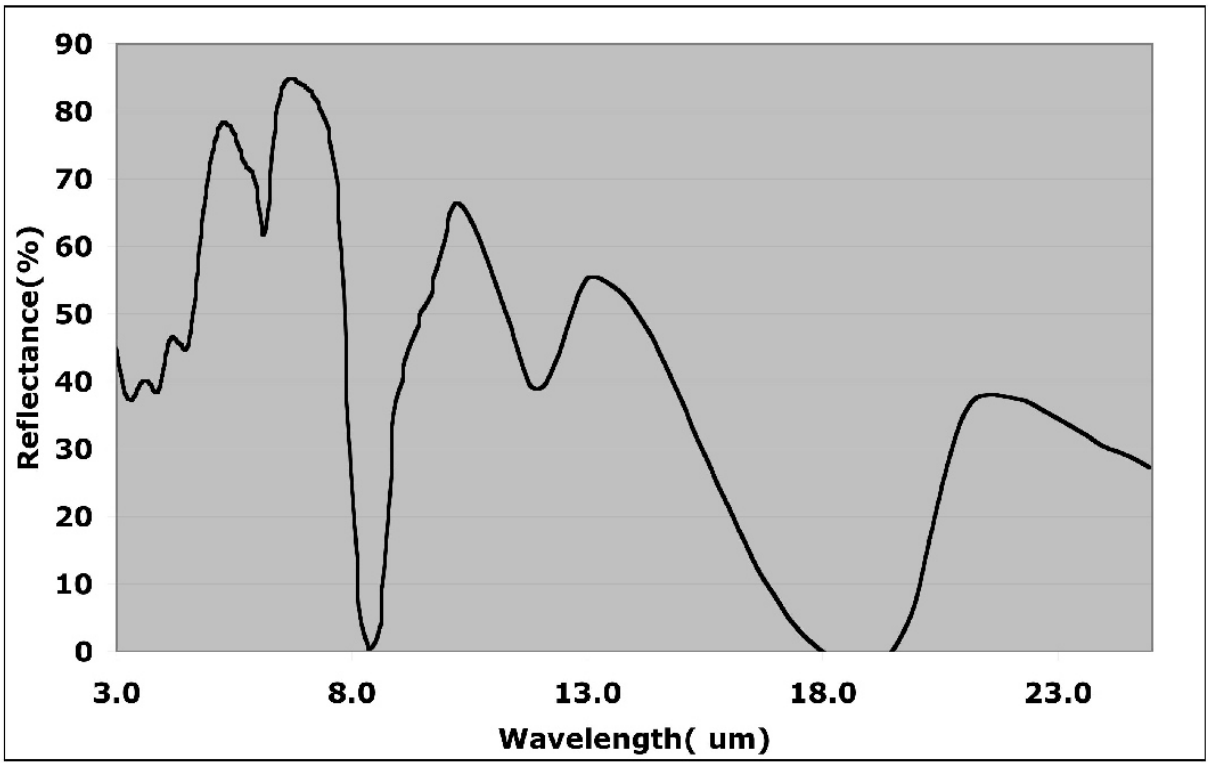

Figure 3.9: Near-normal incidence (7^{o}) reflectance spectrum from 3 layer structure with BCB matrix.

3.3 Characterization

The fabricated structures were characterized by FTIR reflectance spectroscopy. The reflectance spectra of a 3-layer COAC with BCB matrix measured at 7 degree incidence angle for a near normal incidence shows a ~ 80% reflectance between 4.5-8 μm and ~ 55-60% reflectance between 9-15 μm (Figure 3.9). While there is a closer match of the short wavelength band to the RCWA simulation (5-9 μm) the longer wavelength band is considerably more suppressed and narrower and also shows an additional dip near 12 μm. We believe this effect to be arising from absorption the BCB matrix which was not accounted for in the RCWA model. We further analyzed the reflectivity as a function of incidence angles from 7-60 degrees. We found that the shorter wavelength band peak red shifts in addition to splitting into two peaks as the incidence angle is increased while the long wavelength band features remain relatively unchanged (Figure 3.10). This behavior qualitatively agrees with the simulation results.

We also performed reflectivity measurements from an attempted two layer structure with BCB matrix now replaced with PE fabricated using a combination of dry and solvent process. In many places the second layer had delaminated and the reflectivity spectra resulted from a combination of 1 and 2 layer structure (Figure 3.11). Once again the reflectivity spectrum displays expected qualitative behavior.

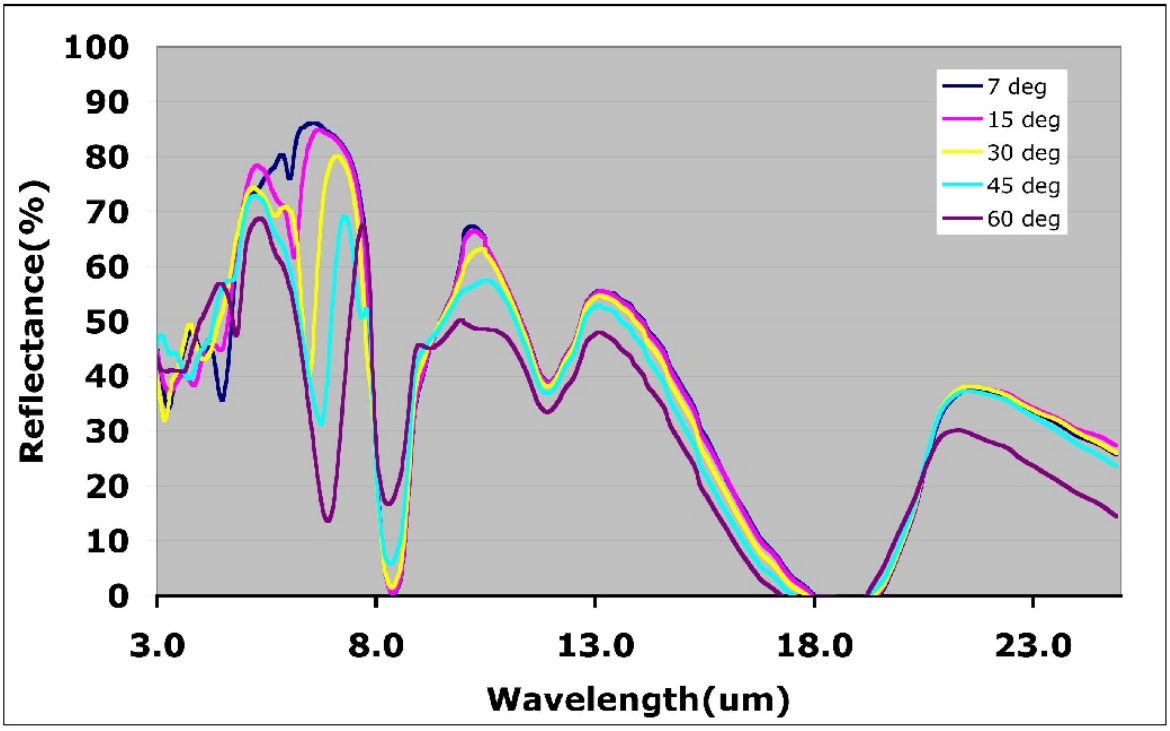

Figure 3.10: Angular dependence of the reflectance spectrum from 3 –layer COAC structure.

The fabrication of the final 3 layer structure using a dry process has been delayed due to CSRL- MESA laboratory transition resulting in prolonged down time and unavailability of the etch tools required to sputter etch the gold cubes. The structures can be fabricated and tested once the necessary etch tools become operational.

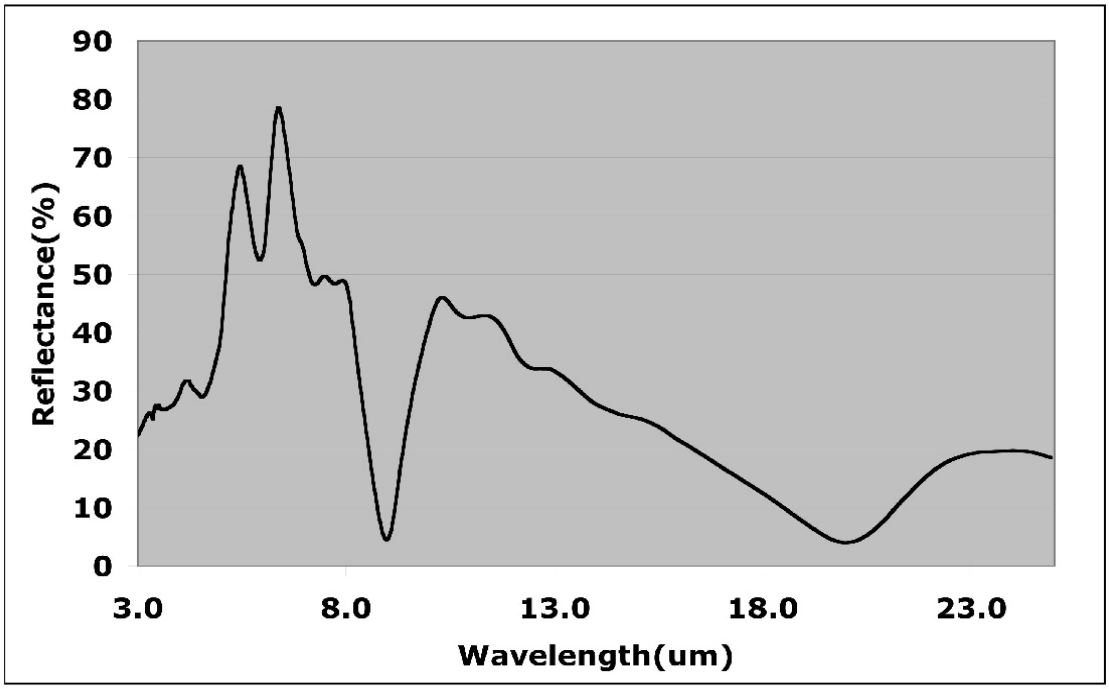

Figure 3.11: Near-normal reflectance spectrum from 2-layer COAC structure with polyethylene matrix.

3.4 References

[1] Stephen Y. Chou, "Nanoimprint Lithography," US Patent #**5772905**, June 30 1998.

[2] S. Y. Chou, P. R. Krauss, W. Zhang, L. J. Guo, and L. Zhuang, " Sub-10nm imprint lithography and and applications", JVST B , **15,** 2897 (1997).

[3]] " Nanoimprint lithography and lithographically induced self-assembly", MRS Bulletin, **26**, 512(2001).

[4] H. Tan, A. Gilbertson, and S. Y. Chou, "Roller nanoimprint lithography", JVST B , **16**, 3926 (1998).

[5] B. Temelkuran, E.L. Thomas, J.D. Joannopoulos and Y.Fink, " Low-loss infrared dielectric material system for broadband dual-range omnidirectional reflectivity", Opt. Lett.,**26**, 1370 (2001). (Figure 3.4a reproduced from publication).

4. Photonic crystal modeling toolsets

In this section we discuss the use of different optimization techniques for finding an optimal PC structure for a predefined/desired spectral plateau. The ability of the proposed method for optimizing PC structures is demonstrated on four spectral plateaus desired to be produced using the well-known Woodpile Lincoln log photonic crystals. It is shown that that such optimization is possible. Our approaches are by no means limited to the Lincoln Log structure, rather this was chosen as a study candidate because of the relatively high success in fabricating it over a wide range of scale lengths. Pros and cons of different optimization methods are discussed and a recommendation to incorporate fuzzy integrals for efficient multi-objective optimization is discussed.

4.1 Introduction

Complex design problems usually involve multi-objective decision making where a choice from a few alternatives that meets overlapping or interrelated objectives shall be made. Multi-objective decision making can thus be dealt with as an optimization problem where trade-offs between objectives is performed by rank ordering alterative solutions according to a pre-defined set of preferences [1]. While theoretical optimization targets finding the global optimum solution (the best optimum solution), practical optimization within the context of multi-objective decision making, targets finding the most optimum solution from a family of reasonable solutions such that the likelihood of meeting the design objective is maximized. Akai [2] showed that exhaustive search can guarantee finding global optimality; however, targeting global optimum or most optimum solution becomes highly dependent on computational resources.

Photonic crystals (PC) are artificial crystals fabricated at the nano scale with the aim of producing materials that have the ability to control light propagation in three dimensions by opening a frequency gap where light cannot propagate [3]. The photonic band structure is created when light encounters a well-defined repeating arrangement of materials with different refractive indices. Such structures can exhibit the property that photons with energy values corresponding to the bandgap cannot penetrate the lattice regardless of their angle of incidence. Interestingly, the photonic properties of PC do not arise from the properties of the materials making up the structure, but mostly from the crystal structure itself [4]. Therefore, it is possible to engineer unique photonic "materials" by controlling the photonic crystal structure. There are three major classes of PC's: One dimensional photonic crystals consist of well controlled variations in refractive index in one dimension enabling the control of light in one dimension. Two dimensional PC's, where the variation of the refractive index is implemented in a two dimensional fashion, are similar thus enabling light propagation control in two dimensions. Finally, three dimensional PC's have well defined variations in refractive index in three dimensions and they make three-dimensional light control possible [4-5]. Obviously, a three dimensional PC is the most complex and target functional PC.

For photonic crystals in the visible to near infrared regimes (400-4000 nm), its smallest necessary size range from 0.1 to 1 micrometer. The relatively small dimensions of PC combined with their complex three dimensional microstructural nature makes fabrication difficult. Recent advances in silicon processing technology, especially chemical-mechanical polishing and micro-

fabrication techniques enabled rapid progress in this area [3,6]. It has been demonstrated that these tools can be successfully applied to the fabrication of PC. The key technologies needed for fabrication are photolithography to define the fine features and chemical mechanical polishing to maintain planarity through the fabrication process. Figure 4.1 shows two exemplar structures of PC lattices fabricated at the nano scale using integrated circuitry production methods. The two examples including the woodpile Lincoln log structure and the cubic array of cubes demonstrate excellent examples for the photonic bandgap that can produce significant enhancement in many engineering applications.

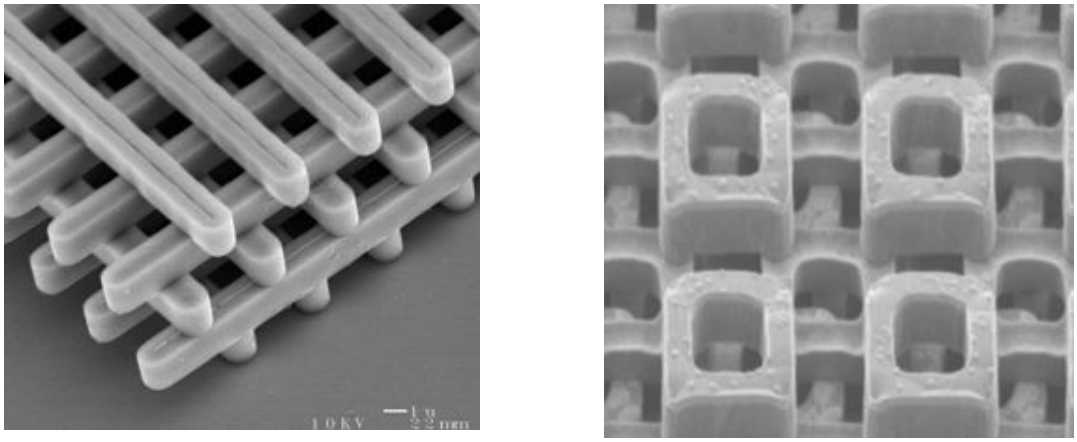

[a] [b]

Figure 4.1: Exemplar photonic crystals with observable bandgaps (a) Licoln log [b] Cubic array of cubes

4.2 Research objectives

The objective of this research is to develop efficient optimization tools to enable optimizing the microstructure periodicity of the PC structure towards an enhanced photonic spectral response. For example, possible alternative microstructures of the Lincoln log woodpile structure similar to those shown in Figure 4.2 might produce photonic responses with different

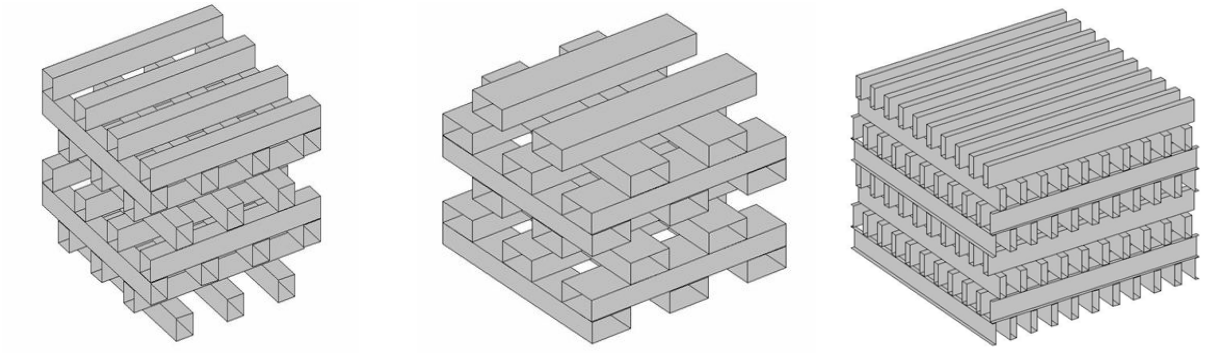

[a] [b] [c]

Figure 4.2: Three possible configurations of Lincoln log photonic crystals showing possible change in microstructure for producing different spectral characteristics.

characteristics.

The objective of the optimization process is to find a unique microstructure of the photonic lattice defined by defining the three fundamental geometrical dimensions of the Woodpile Lincoln log PC including the lattice constant (a), the woodpile rod width (w) and the woodpile rod height (h) as shown in Figure 4.3. The optimized microstructure shall be able to produce a desired photonic response including reflection, transmission or absorption.

Such development can have an immense effect on the design and choice of the photonic lattice for thermophotovoltaics emitter applications, frequency up-converters, and compact optical systems.

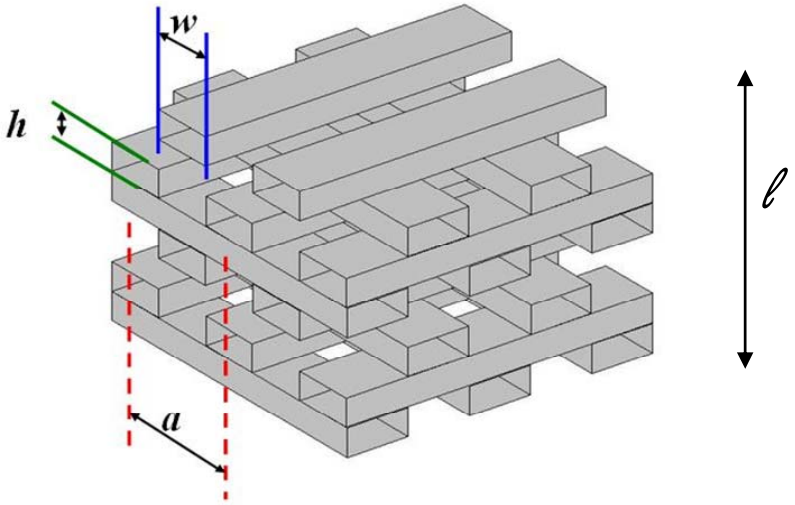

Figure 4.3: Design variables of the PC including the lattice constant (a), the woodpile rod width (w), woodpile rod height (h) and number of layers (l).

The challenge in producing such optimal structures is the absence of a set of closed-form mathematical functions of the photonic spectral-microstructure relationship. Here we describe the methods used to simulate the photonic spectral response of the PC and the methods that can be used for system optimization. An integrative optimization module is described and some preliminary results showing the ability of the proposed model to collapse to optimal yet constructible photonic crystals.

4.3 Methods

4.3.1 PC Spectral Simulation Techniques

Researchers [7-9] showed that simulation of the photonic spectral response (reflection, absorption and transmission) of the photonic crystal requires solving Maxwell's equations that govern electromagnetic wave propagation

$$\nabla \times \mathbf{H} = \varepsilon_0 \varepsilon(\vec{r}) \frac{\partial \mathbf{E}}{\partial t}$$
$$\nabla \times \mathbf{E} = -\mu_0 \mu(\vec{r}) \frac{\partial \mathbf{H}}{\partial t} \quad (1)$$

where E is the electric field vector, H is the magnetic field vector, $_0$ and $_0$ are the free space permittivity and permeability constants, and are the permittivity and permeability of the photonic lattice [7-8]. Several numerical methods have been nominated to solve Maxwell's Equations particularly the Finite Difference Time Domain (FDTD), Transfer Matrix Method (TMM) and Modal Expansion Method (MEM) [10].

The Finite Difference Time Domain (FDTD) method is a numerical technique which is based on direct integration of Maxwell's Equations [11]. In order to apply this technique, the spatial and temporal derivatives in Maxwell's Equations are converted to finite differences on a grid mesh, discretizing the structure at hand. The method yields electromagnetic fields in space and time as the desired solution. Post-processing including Fourier Transform is applied to change to frequency domain and obtain transmission and reflection coefficients. A single FDTD run can yield a complete spectrum of transmission and reflection coefficients, making FDTD a very efficient method. Although FDTD is also a robust and well-tested method, it cannot handle dispersive materials such as metals naturally. Since the structure of interest is a metallic structure, FDTD does not constitute the best choice in this case.

The Transfer Matrix Method (TMM) generates a "transfer matrix" which relates electromagnetic fields at one side of a structure to the fields at the other side. Such a transfer matrix provides a summary of the electromagnetic properties of the structure it covers [12]. In order to obtain a matrix in mathematical sense, which can be used on a computer, it is necessary to discretize the structure. Unlike FDTD however, TMM does not convert temporal derivatives to finite differences. Instead, it eliminates temporal derivatives by assuming plane wave propagation at a single frequency, making TMM a frequency domain method. Calculation of transmission and reflection coefficients is performed by sending in principal modes of light propagating in free space through the structure (transfer matrix). The actions of the transfer matrix on these modes are sufficient to calculate the desired coefficients. In order to obtain spectra, it is necessary to repeat TMM calculations using different frequencies in the frequency range of interest. Although numerical calculation of the principal modes is possible in theory, a semi-analytical method is frequently used in practice due to instabilities with the former. TMM can simulate dispersive materials naturally; however, it suffers from an inherent numerical instability due to the formulation of the transfer matrix. The instability causes some elements of the transfer matrix to grow exponentially while other elements decay exponentially, rendering

linear algebra operations with the transfer matrix unreliable. Therefore, TMM was not our method of choice.

The Modal Expansion Method (MEM) is similar to TMM, with three differences: Firstly, MEM uses a different discretization scheme for Maxwell's Equations: First a Fourier Transform is applied to obtain Maxwell's Equations in frequency domain, and series expansion is utilized next [13]. Secondly, MEM does not require the usage of principal light modes in order to obtain transmission and reflection spectra. Finally, MEM uses a different transfer matrix formulation to eliminate the numerical instability inherent in TMM. Since the discretization is in Fourier domain, MEM is able to simulate periodic structures very accurately with very few series elements. Additionally, MEM is able to simulate dispersive materials accurately thanks to its frequency domain nature.

The Rigorous Coupled Wave Analysis (RCWA) method employed in our tests is another numerical technique which is related to Transfer Matrix Method and Modal Expansion Method [14]. RCWA method is specifically developed for diffraction gratings, and has been successfully employed for various types of diffraction gratings for several decades. Since the rod layers of the Lincoln-log structure can be considered as gratings individually, a numerical method optimized for diffraction gratings, namely RCWA, is able to solve electromagnetic field equations for the Lincoln-log structure. Like MEM, RCWA starts from Maxwell's Equations in Fourier domain,

$$\begin{aligned} j\vec{k}\times\vec{E} &= j\omega\mu\vec{H} \\ j\vec{k}\times\vec{H} &= -j\omega\varepsilon\vec{E} \end{aligned} \tag{2}$$

where E is the electric field vector, H is the magnetic field vector, and are parameters describing the electromagnetic properties of the structure of interest, is the angular frequency, and k is the wave number for the electromagnetic wave. RCWA expands E, H and in series expansions,

$$\begin{aligned} \vec{\mathrm{E}}(\vec{\mathrm{r}}) &= \sum_{\mathrm{mn}}^{\mathrm{MN}} \mathrm{E}_{\mathrm{mn}}(z) e^{j(k_{mn,x}x+k_{mn,y}y)} \\ \vec{\mathrm{H}}(\vec{\mathrm{r}}) &= \sum_{\mathrm{mn}}^{\mathrm{MN}} H_{\mathrm{mn}}(z) e^{j(k_{mn,x}x+k_{mn,y}y)} \\ \varepsilon(\vec{r}) &= \sum_{\mathrm{mn}}^{\mathrm{MN}} \varepsilon_{\mathrm{mn}}(z) e^{j\vec{G}_{mn}\cdot\vec{r}} \end{aligned} \tag{3}$$

and arranges the system of equations into a matrix form. In the matrix form, electromagnetic field components are grouped according to their locations and propagation directions. Field components at the two sides of the grating are posed as vectors related to each other by means of a transfer matrix. Define a vector of fields, F,

$$F = \begin{Bmatrix} E_x \\ E_y \\ H_x \\ H_y \end{Bmatrix} \tag{4}$$

F has a superscript denoting whether the fields are located at the *left* (-) or *right* (+) side of the grating and a subscript indicating whether the fields are directed to *left* (-) or *right* (+). One can define the transfer matrix called the scattering matrix (S) as

$$\begin{bmatrix} F_r^r \\ F_l^l \end{bmatrix} = (S) \begin{bmatrix} F_r^l \\ F_l^r \end{bmatrix} \tag{5}$$

The scattering matrix is used to connect the electromagnetic fields *coming towards* the grating to the fields *propagating away* from it. The S matrix can be used for calculation of transmission and reflection coefficients by simply requiring electromagnetic fields will be incident on the structure one side at a time. One can immediately write,

$$\begin{bmatrix} F_{ref} \\ F_{trans} \end{bmatrix} = (S) \begin{bmatrix} 0 \\ F_{inc} \end{bmatrix} \tag{6}$$

In order to calculate the overall S matrix for stacked layers of gratings as well as the Lincoln-log structure out of the S matrices for individual layers, recursion formulas are used. For the sake of brevity, recursion formulas and other details of the RCWA method is not included in this document but can be found elsewhere [14].

4.3.2 The Optimization Process

The optimization process of any system can be classified by defining three major components being: the optimization parameters, the optimization (*objective*) function, the system constraints and the optimization method.

Design variables

The design variables here are the variables that control the lattice microstructure including the lattice constant (a), the rod width (w) and the rod height (h). The design variables of the PC are shown before in Figure 4.3. In addition, the angle of incident (α) can also be considered as a design variable. While the analysis described here is limited to the first three design variables, the optimization process has been established to incorporate the angle of incident as well.

Design parameters

The design parameters are those parameters necessary for the simulation process but are not part of the optimization process. They are essential as they are needed for the simulation but they do not play any major role in defining the optimal microstructure. Such parameters include the physical characteristics of the material (e.g. permittivity) and the number of layers of the PC.

Design functions

The design functions are the functions used for system simulation. Here the RCWA model is the design function. The RCWA simulation was developed using GD-CALC™ [15] module in MATLAB® [16] environment. The design functions require the design variables and the design parameters to operate. The optimal solution is based on the design function is not also dependent on other constraints and desired performances. The output of the design function here includes the optimal reflectance, absorption and transmission. A schematic representation of the design variables and design parameters and their feed to the RCWA as a design function is illustrated in Figure 4.4.

Objective function

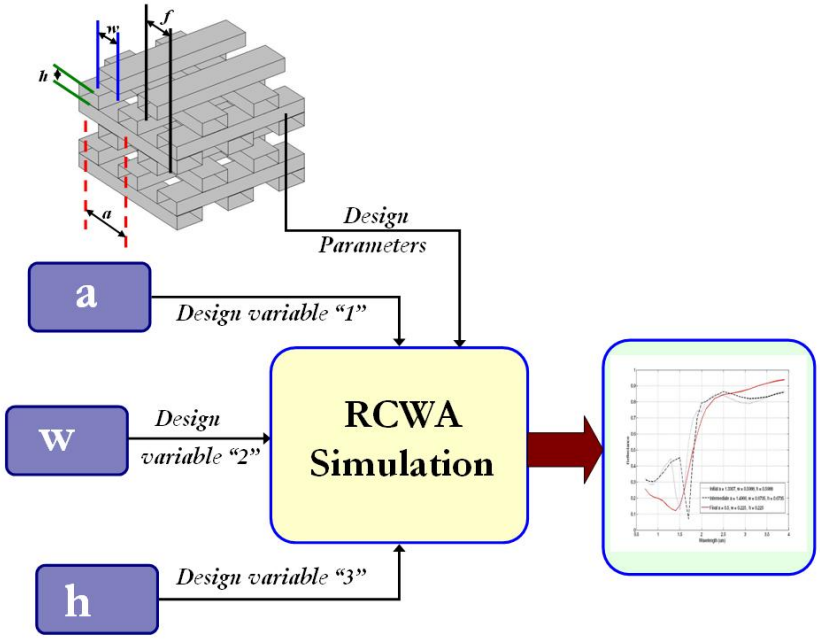

Figure 4.4: Schematic representation of the design variables and design parameters and their rules in creating the spectral simulation and the objective function.

Traditionally, optimization problems are set by defining a single objective function. In such problem the global minimum or maximum of this function is searched. However, practically speaking the problem in hand might fall within the definition of multi-objective optimization. To explain: the objective function shall be able to maximize one of the spectral characteristics (e.g. reflectance) within a predefined wavelength domain while minimizing other spectral characteristics (e.g. absorption) within another wavelength domain. The two objectives might not be necessary mutually exclusive but can be interestingly conflicting. We discuss here first the techniques achieve the desired optimization of the objective function over one domain; we then discuss techniques for multi-objective optimization.

We start by defining a generic objective function that can be used for optimizing the three possible target spectral responses of the PC including the reflection, the absorption and the transmission. In all cases, the objective will be maximizing the response of interest such that it reaches 100% within a specific wavelength interval. The response outside the zone of interest shall be zero. We therefore define the optimal response profile as shown in Figure 4.5. The desired spectral plateau function can be defined as

$$f_{desired}(\lambda) = \begin{cases} 0 & \lambda_{min} \le \lambda \le \lambda_1 \\ 1 & \lambda_1 \le \lambda \le \lambda_2 \\ 0 & \lambda_2 \le \lambda \le \lambda_{max} \end{cases} \qquad (7)$$

where $f_{desired}(\lambda)$ is the desired spectral response at the wavelength (λ), and λ_{min}, λ_{max} are the limits of the wavelength interval of interest while λ_1 and λ_2 define the borders of the bandgap zone. We then define the simulation model output at the wavelength λ as $f(a,w,h,\lambda)$ which can be denoted for simplicity as $f(\lambda)$. Given the optimization objective to maximize the spectral response of the PC within the bandgap zone, the objective function $E(a,w,h,\lambda)$ which can also be denoted for simplicity as $E(\lambda)$ can be defined as

$$E(\lambda)=\sqrt{\frac{\eta_1.\Delta\lambda_1}{\lambda_1-\lambda_{min}}\sum_{\lambda=\lambda_{min}}^{\lambda_1}\left(f(\lambda)\right)^2+\frac{\eta_2.\Delta\lambda_2}{\lambda_2-\lambda_1}\sum_{\lambda=\lambda_1}^{\lambda_2}\left(f_{desired}(\lambda)-f(\lambda)\right)^2+\frac{\eta_3.\Delta\lambda_3}{\lambda_{max}-\lambda_2}\sum_{\lambda=\lambda_2}^{\lambda_{max}}\left(f(\lambda)\right)^2} \quad (8)$$

Where $\Delta\lambda_1$, $\Delta\lambda_2$ and $\Delta\lambda_3$ are the discrete wavelength step sizes defined over the three zones shown in Figure 4.5 between (λ_{min}, λ_1), (λ_1, λ_2), (λ_2, λ_{max}) and η_1, η_2 and η_3 represents numerical weights.

The change of the wavelength step size proved necessary for limiting the computational expenses of the simulation model. In other words, this gives the opportunity to change the resolution of computations within each step on the basis of the importance of these regions on the decision process. The use of weights is another interesting factor proved necessary for multi-objective optimization. While other definitions of the objective function are possible, we limit the discussion of this article on investigating, the pros and cons of the proposed objective functions. Other objective functions based on principles of fuzzy multi-objective decision making are being sought and will be examined. A schematic representation showing the optimization module integrating the RCWA simulation module is shown in Figure 4.6

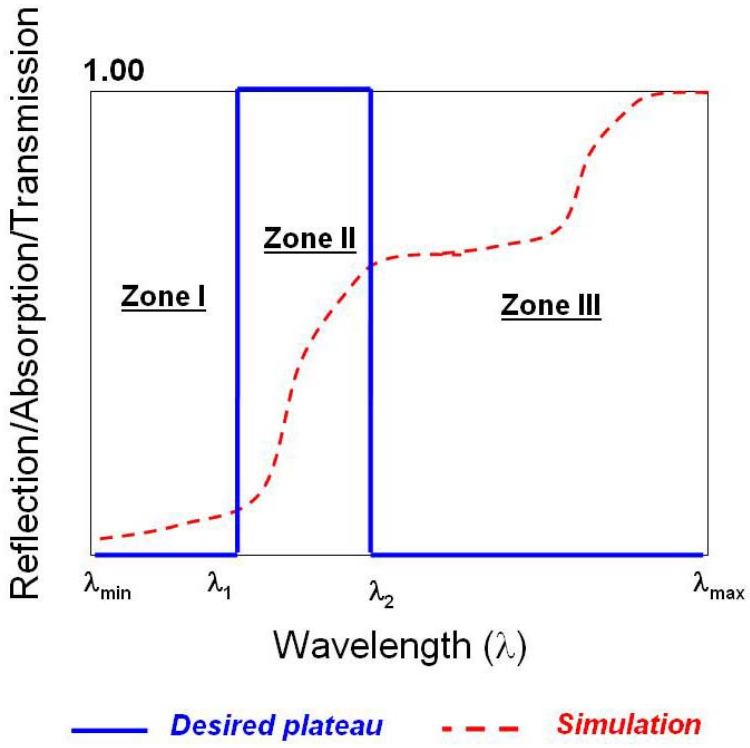

Figure 4.5: Schematic representation of the desired plateau and a typical simulation output showing the division of the wavelength domain into three zones. Zone II is always the zone of interest.

Optimization constraints

To produce manufacturable photonic crystals, constrained optimization was necessary to impose nano fabrication limits. Such constraints included the minimum possible thickness and width dimensions of the woodpile rod, the inequality constraints necessary to ensure appropriate aspect ratios of the rod dimensions and their relation to the lattice constant. It is important to emphasize that such inequality constraints are problem specific and shall be defined before any optimization algorithms to be employed.

Optimization techniques

It is well established that two groups of optimization techniques can be employed for multi-dimensional constrained optimization problems. These groups are: derivative-based and derivative-free optimization [17-19]. Each group has its advantages and disadvantages but both are much dependent on the shape of the objective function and the nature of local and global minima in this function. This depicts the fact that function continuity and the nature of local minima and their distribution adds to the optimization challenges represented by the need to limit computation expenses and to ensure the practicality of the proposed design variables.

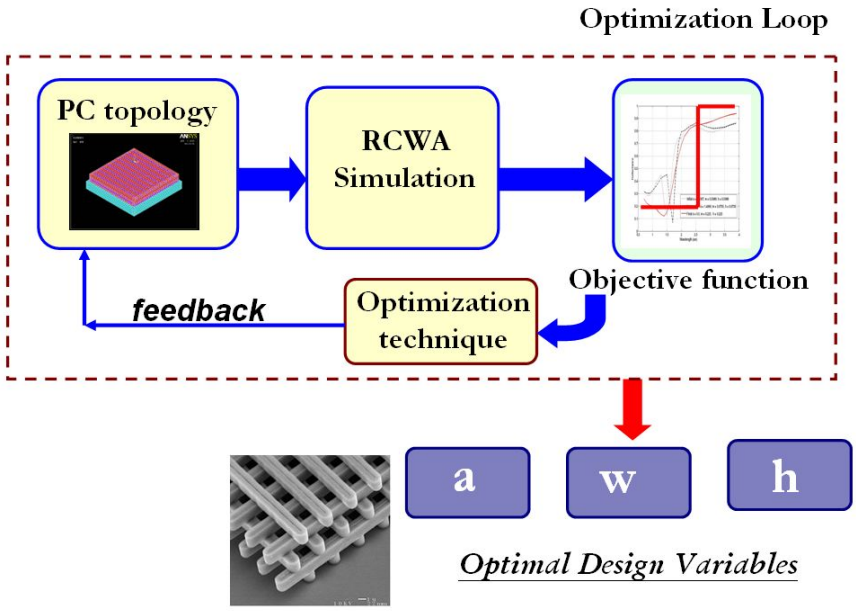

Figure 4.6: Optimization loop showing simulation of photonic spectral using RCWA and the process to optimize the PC structure for a desired response plateau.

Derivative-based optimization includes optimization techniques such as Netwon-Raphson, Golden section and Fibonacci for single variable optimization and parallel tangents and steepest gradients for multi-variate optimization [20]. These techniques usually showed good success when the number of local minima is limited and the function can be described in a closed form mathematical expression. Derivative-based optimization techniques depend on recognizing the direction of the derivative if the function is known or the gradient if the function is unknown. On the other hand, derivative-free optimization techniques (such as genetic algorithms and simulated annealing) are alternative techniques that do not depend on the gradient information but strives to find the global minimums through exhaustive search mechanisms [21]. While derivative-free optimization techniques represent the best alternative when a considerable number of local minima exist, they represent a computationally expensive solution compared with derivative-based when local and global mimina coincide. Here, we describe three techniques employed in the PC optimization process. Those techniques include the multi-variate gradient descent technique and Levenberg-Marquardt as derivative-based optimization techniques and the genetic algorithm (GA) as derivative-free optimization technique.

Gradient Descent Method

It is well-established that finding the local minimum of a function $E(X)$, where X is a vector of design variables can be achieved if the function is differentiable over the search space

or if a numerical approximation of the gradient can be computed. The technique is based on the possible update of the design variables vector X_{i+1} given an educated guess X_i

$$X_{i+1} = X_i - \alpha\, G\, g \tag{9}$$

Where g is the gradient of the objective function, G is a positive definite matrix and α is a positive step size. The gradient of the objective function g is defined as

$$g(x) = \left[\frac{\partial E(x)}{\partial x_1} \quad \frac{\partial E(x)}{\partial x_2} \quad .... \quad \frac{\partial E(x)}{\partial x_n} \right]^T \tag{10}$$

These iterations are carried out typically until the gradient approaches zero which indicates a local minima to exist. The analysis and its stability is strongly dependent on the parameter α which might actually control the rate of convergence of the algorithm. Bad choices of α might result in oscillatory behavior [23].

<u>Levenberg-Marquardt (LMA) Method</u>

The Levenberg-Marquardt (LMA) method can be considered as modified version of classical Newton's method [24-26]. It assumes continuous and differentiable function or a function for which gradient can be evaluated numerically. Let X_i be the initial educated guess of the design variable vector X. Using LMA an updated vector of the design variable X_{i+1} can be defined as

$$X_{i+1} = X_i - \alpha\, \left(H + \lambda\, I\, \right)^{-1} g \tag{11}$$

where g is the gradient defined in Equation (10), I is the identity matrix, λ is some nonnegative value, α is a positive step size and H is the Hessian matrix defined as

$$H(x) = \left[\frac{\partial^2 E(x)}{\partial x_1^2} \quad \frac{\partial^2 E(x)}{\partial x_{2_2}^2} \quad .... \quad \frac{\partial^2 E(x)}{\partial x_n^2} \right]^T \tag{12}$$

While equation (12) provides the generalized form for the LMA technique for gradient based optimization, LMA can be very efficiently used in the form of non-linear least-squares which is similar to the objective function defined in Equation (8). In this context, LMA can be defined as

$$X_{i+1} = X_i - \left(J^T\, J + \lambda\, I\, \right)^{-1} g \tag{13}$$

Where J is the Jacobian matrix of the residual "r" defined from the gradient g or the Hessian matrix H as

$$H = 2(J^T\, J + S) \tag{14}$$

$$S = \sum_{i=1}^{m} r_i(x) \frac{\partial^2 r_i(x)}{\partial x \quad \partial x^T} \tag{15}$$

The (non-negative) damping factor is adjusted at each iteration for fast convergence. If the residual error is getting reduced quickly, then a relatively small one shall be used while a

relatively high one is needed is the residual error (S) is reduced slowly. The ability of the LMA to enhance the speed of convergence of the optimization process compared to other derivative-based methods is attributed to its ability to regulate the direction of the descent and update it during optimization by controlling the damping factor λ. Figure 4.7 shows the location of LMA descent with respect to the original Newton's descent and that of the steepest descent method.

Derivative-Free Optimization

While bound to be generally slower than derivative-based methods, derivative free optimization methods have shown a great deal of flexibility and robustness. Derivative free optimization methods are based on intuitive ideas. Two methods have been well received by the scientific communities and showed numerous cases of success. This includes genetic algorithms (GA) and the simulated annealing (SA) [24-26]. GA and SA have proved useful in many optimization problems where conventional methods like gradient climbing or simplex have failed due to the inherent complexity of the problem. Here we explain the basic principles of GA and use it as a derivative free optimization technique for finding an optimal photonic crystal.

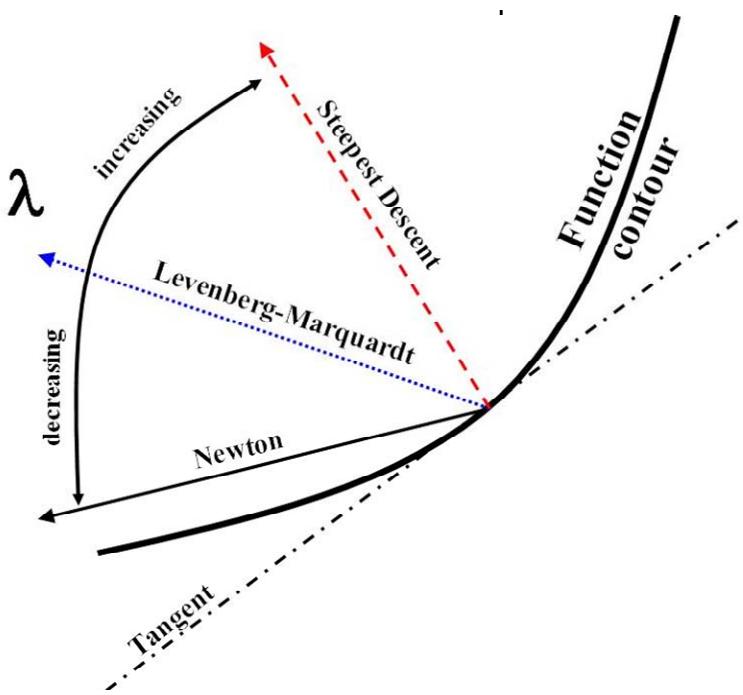

Figure 4.7: LMA's descent (blue-dotted) compared with Newton's gradient (solid-black) and steepest descent direction (dashed-red) showing the ability of the damping factor l to regulate LMA's descent leading to a relatively faster convergence compared with derivate-based methods [19].

Genetic algorithms are based on the process of natural evolution, where organisms adapt to their environment or become better suited for survival over many generations of mutations, reproductions and genetic crossovers [27]. Natural selection determines which members of the population survive and reproduce. Similarly, in evolutionary computation, system optimization requires that weed out badly performing solutions in the process of natural selection. This usually entails testing if the solution meets a certain performance criteria or meets a cost function. The crossover and mutation processes are usually carried out on strings that represent the chromosomes of each individual solution. These tend to be usually binary strings for ease of manipulations but need not be restricted to a binary representation [27, 28]. The fact that GA requires little information about the function to optimize makes GA an excellent candidate to perform the optimization process in hand

Genetic Algorithms are performed in four stages. These are evaluation, selection, crossover and mutation. The evaluation procedure measures the fitness of each individual solution in the population and assigns it a relative value based on the defining optimization (or

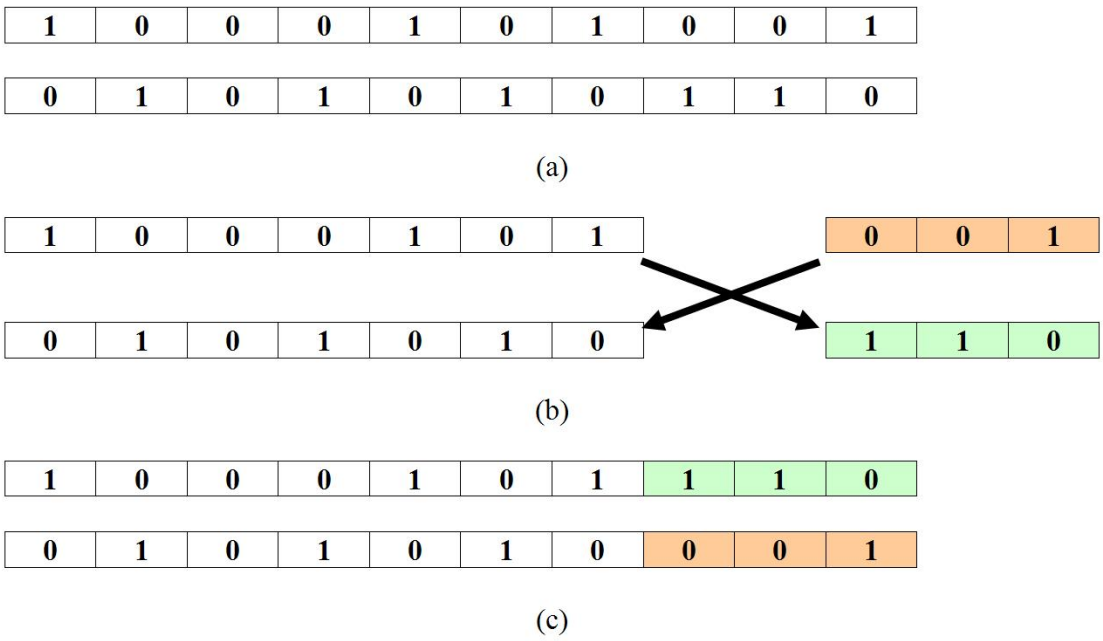

Figure 4.8: The crossover process explained on the basis of binary definition of strings (a) Two randomly selected strings (b) randomly located portions (c) portions are exchanged

search) criteria. Typically in a non-linear programming scenario, this measure will reflect the objective value of the given model. The selection procedure randomly selects individuals of the current population for development of the next generation. The crossover procedure takes two selected individuals and combines them about a crossover point thereby creating two new individuals [21,28]. Schematic representation of the crossover procedure in a binary format is depicted in Figure 4.8. The mutation procedure randomly modifies the genes of an individual subject to a small mutation factor, introducing further randomness into the population. The mutation process is represented in Figure 4.9.

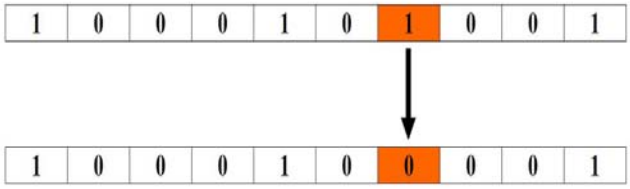

Figure 4.9: Schematic representation of mutation process [29].

This iterative process continues until one of the possible termination criteria is met: if a known optimal or acceptable solution level is attained; or if a maximum number of generations have been performed; or if a given number of generations without fitness improvement occur.

4.4 Photonic Crystal Multi-pixel Design

In this section we describe a unique hybrid optimization technique based on Genetic Algorithms (GA) and Gradient Descent (GD) methods for smart design of photonic crystal emitters that was developed under this LDRD. We describe the photonic simulation method and consider the granularity of the photonic crystal dimensions that controls the design of the emitter. We demonstrate an innovative sliding window method for local heuristic search and show how the proposed method improves the convergence rate of the optimization process. We also implement a technique for caching spectral simulations and demonstrate how the caching becomes indispensable in an optimization process that has a computationally expensive objective evaluation routine.

Finally, we demonstrate the application of the proposed method on a case study for the design of a multi-pixel photonic emitter made of four independent Tungsten Lincoln-log photonic crystals. With the implementation of our unique optimization methods, an average emitter efficiency of 50% is achieved over a wide range of infrared wavelengths is achieved. We specially note the unprecedented high emitter efficiency of 55% at a significantly long wavelength region.

4.4.1 Problem Statement

Our objective is to develop a robust method that can identify the parameters describing the lattice microstructure of a photonic crystal, for a given spectral response. Here, we discuss the use of photonic crystals in a multi-pixel system as schematically shown in Figure 4.10. Each pixel may be used independently or simultaneously such that the multi-pixel photonic system can manipulate the photonic absorption response over a relatively broad spectrum (1 to 10 μm wavelength). As an example, a set of five different photonic crystals with different emission properties could be stacked on top of each other to recycle and emit energies across a wide range of wavelengths (Figure 4.1(a)). In another instance, they could be employed as juxtaposed pixels operating in four distinct wavelength regions, as shown in Figure 4.1(b). The objective is to control light absorption within this wide window of wavelengths based on the ability of PCs to manipulate light in three dimensions [34]. By designing each photonic crystal pixel independently for distinct wavelength regions, the target absorption response for the entire wavelength range in question can be controlled.

We assume here that several PCs designed independently can be fabricated together in the required final format as a single unit without modifying their individual expected behavior. While we limit our discussion here to Lincoln-log woodpile metallic crystals (Figure 4.1a), we claim that the behavior of the proposed optimization techniques and methods to be quite invariant with respect to the material and geometry used and expect these methods to be extendable to other PC geometries and materials with little or no modification. A schematic of a Lincoln-log photonic crystal with its design parameters, Tungsten characteristics number of layers (l), and design variables, namely, lattice constant (a), rod width (w), and rod height (h) are shown in Figure 4.3.

Classical design processes tend to be based on trial and error, estimates based on expert opinions and fabrication constraints. There are several problems with such an approach. First, the time needed for photonic crystal simulation for one set of design variables on a typical desktop computer is considerably long (2 hours). Second, the space of such estimates is quite large and is filled with several non-linearities. A single incremental change in one of the variables sometimes tends to give an unexpectedly superior or inferior response. The process gets further complicated with the fact that several PC pixels and not just one need to be designed. Also, a considerable challenge exists in the long wavelength region for metals, especially those known to have low-absorption (e.g. Tungsten has 0.3% absorption at long wavelengths), in which case a considerably flat PC

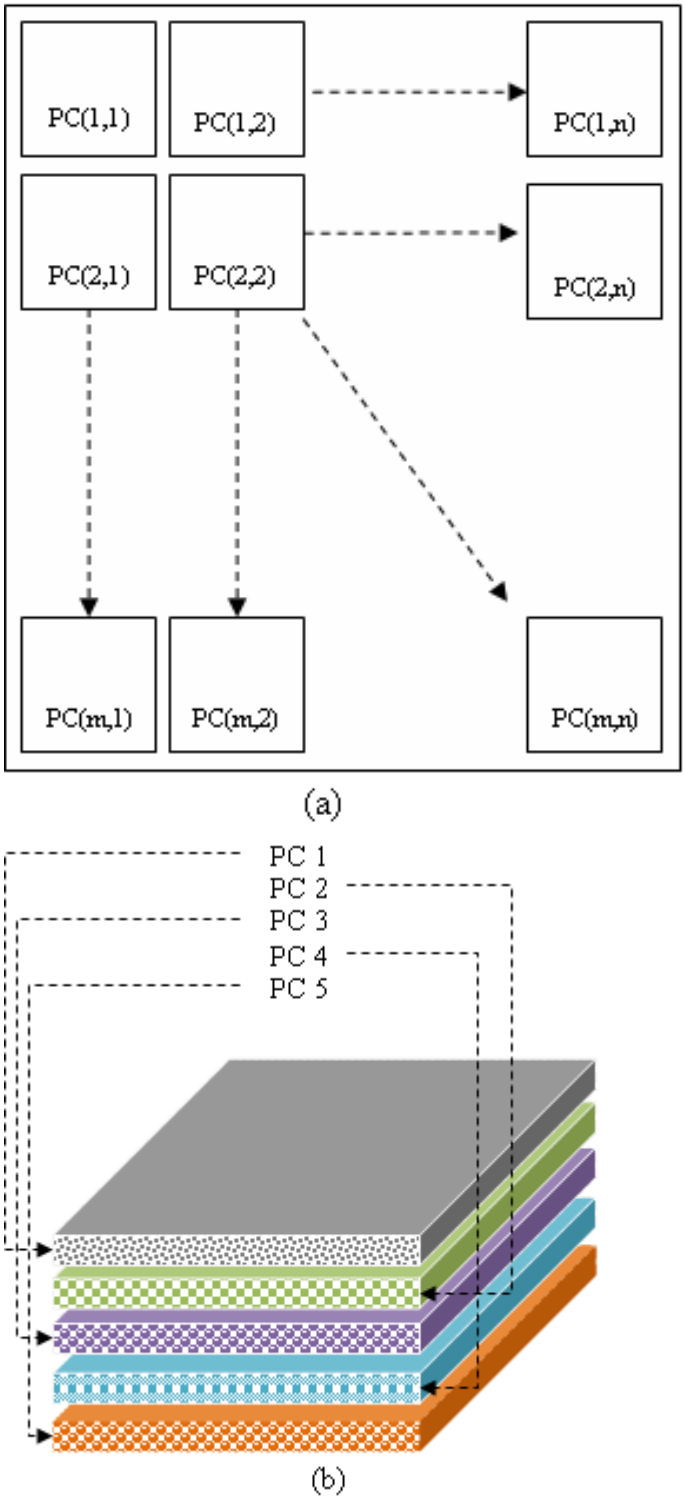

Figure 4.10: Two examples of multi-pixel photonic crystal systems. (a) An $n \times m$ grid of individual crystals on a common substrate. (b) A 5-layer heterogeneous, multi-material, multi-geometry stack of photonic crystals.

dispersion is needed to ensure a sufficiently small group velocity and hence provide the necessary absorption via the prolonged light-matter (PC) interaction time. To provide a perspective, the problem at hand could be classified as constrained discrete optimization. Computationally, we can readily see that problem is worst case bounded by Integer Linear Programming (ILP) assuming that the objective function is at best linear. Hence, the problem can be considered as an NP-hard problem [43].

4.4.2 Adopted Methods

4.4.2.1 Photonic Simulation

In this section, we will describe the computational theory to simulate the spectral behavior of the photonic crystal for a known geometry. There is an abundance of numerical methods available for PC simulation, these include: finite difference time domain [40], Green's function integral equations [42], the transfer matrix methods [43] and the modal expansion method [44]. All these methods possess advantages and disadvantages alike. In this paper; however, our focus is directed towards the iterative optimization technique that would enable the prediction of the most suitable PC design given a predefined spectral response. As such we are not biased to one method over the other, what we are interested primarily in is a fast, accurate method for the generation of the test cases. Because of the topological structure of the Lincolin Log PC lattice that can be reduced to successive layers of two dimensional grating structures, we chose to perform the test calculations using Rigorous Coupled Wave Analysis (RCWA) technique [45], however our results and methods still hold independently of that choice, and would be equally valid had we chosen an alternate computational technique to generate the test cases.

The RCWA method starts from Maxwell's Equations in Fourier domain, as

$$\begin{aligned} j\vec{k}\times\vec{E} &= j\omega\mu\vec{H} \\ j\vec{k}\times\vec{H} &= -j\omega\varepsilon\vec{E} \end{aligned} \tag{1}$$

where E is the electric field vector, H is the magnetic field vector, and are parameters describing the electromagnetic properties of the structure of interest, is the angular frequency, and k is the wave number for the electromagnetic wave.

E, H and are then expressed as a series expansions, and the system of equations are arranged into a matrix form. In matrix form, electromagnetic field components are grouped according to their locations and propagation directions. Field components at the two sides of the grating are posed as vectors related to each other by means of a transfer matrix and can be expanded as,

$$\begin{aligned} \vec{\mathrm{E}}(\vec{\mathrm{r}}) &= \sum_{\mathrm{mn}}^{\mathrm{MN}} \mathrm{E}_{\mathrm{mn}}(z) e^{j(k_{mn,x}x + k_{mn,y}y)} \\ \vec{\mathrm{H}}(\vec{\mathrm{r}}) &= \sum_{\mathrm{mn}}^{\mathrm{MN}} H_{\mathrm{mn}}(z) e^{j(k_{mn,x}x + k_{mn,y}y)} \\ \varepsilon(\vec{r}) &= \sum_{\mathrm{mn}}^{\mathrm{MN}} \varepsilon_{\mathrm{mn}}(z) e^{j\vec{G}_{mn}\cdot\vec{r}} \end{aligned} \tag{2}$$

If we now define a vector of fields, F. as:

$$F = \begin{Bmatrix} E_x \\ E_y \\ H_x \\ H_y \end{Bmatrix} \tag{3}$$

and let the superscript (*l/r*) for F denote whether the fields are located at the *left* (-) or *right* (+) side of the grating and the subscript (*l/r*) indicating whether the fields are directed to *left* (-) or *right* (+), then one can define the transfer matrix called the scattering matrix (S) [34,36] as,

$$\begin{bmatrix} F_r^r \\ F_l^l \end{bmatrix} = (S) \begin{bmatrix} F_r^l \\ F_l^r \end{bmatrix} \tag{4}$$

The scattering matrix is used to connect the electromagnetic fields *coming towards* the grating to the fields *propagating away* from it [34, 36]. The S matrix can be used for calculation of transmission and reflection coefficients by simply requiring that the electromagnetic fields be incident on the structure one side at a time. Therefore,

$$\begin{bmatrix} F_{ref} \\ F_{trans} \end{bmatrix} = (S) \begin{bmatrix} 0 \\ F_{inc} \end{bmatrix} \tag{5}$$

In order to calculate the overall S matrix for stacked layers of gratings such as the Lincoln-log structure out of the S matrices for individual layers, recursion formulas are used [34, 36]. For the sake of brevity, recursion formulas and other details of the RCWA method are not included in this paper but can be found elsewhere [34-37].

We developed the simulation in the MATLAB® programming environment using the GD-CALC™ module. The input to the computational environment is the crystals geometry, and material properties. The simulation results providing numerical approximation of the spectral responses of the photonic crystal. These responses include the reflectance, absorption and transmission responses from the PC pixel to a range of normally incident monochromatic EM radiation frequencies. A schematic representation of the design variables and design parameters as input to the RCWA simulation as a design function is illustrated in Figure 4.4.

4.4.2.2 PC Optimization

Before describing the optimization problem in detail in the following sections, we will define some important terms, namely *design variables*, *design parameters* and *design constraints*. We define the design variables as *n-tuple* of variables ‹x_1, x_2, ..., x_n›, where each variable in the tuple is an independent variable subject to the *design constraints*. Specifically, a Lincoln-log photonic crystal has three design variables, and =‹*a*, *w*, *h*›, where *a* is the lattice constant, *w* is rod width and *h* is the height of the rods (Figure 4.4.). *Design parameters* are quantities that remain fixed throughout the optimization process, but are still crucial in simulating the response of the photonic crystal. Material emissivity ( ) and the number of layers (ℓ) are two design parameters for the Lincoln-log crystal. *Design constraints* are the set of constraints that are imposed on the *design variables* to ensure a practical and realistic design.

4.4.2.3 The Objective function

The objective of the optimization process is to identify the photonic crystal variables that can maximize the absorption and transmission (emission) profiles within a specific wavelength window for a PC. Let the combined transmission and absorption profile of the photonic crystal at wavelength , be denoted TA, which can simply be written as the portion of incident radiation that is not reflected, R.

$$TA(\lambda) = 1 - R(\lambda) \tag{6}$$

With this definition, the objective is to maximize the TA profile within a pre-specified wavelength window. This objective can be achieved by manipulating the design variables *a*, *w* and *h*. An example representation of the simulated TA response versus the desired TA plateau is shown in Figure 4.5.

Defining the desired TA profile as,

$$TA_{desired}(\lambda) = \begin{cases} 0 & \lambda_{min} \le \lambda \le \lambda_1 \\ 1 & \lambda_1 \le \lambda \le \lambda_2 \\ 0 & \lambda_2 \le \lambda \le \lambda_{max} \end{cases} \tag{7}$$

$TA_{desired}(\lambda)$ is the desired spectral response at the wavelength (λ), $_{min}$ and $_{max}$ are the limits of the wavelength interval of interest while $_1$ and $_2$ define the borders of the bandgap zone. We then define the simulation model output at the wavelength of interest as $f(a,w,h,\lambda)$ which can be denoted for simplicity as $f(x\ ,\ )$, where x is the *triplet* of variables ‹*a*, *w*, *h*›. Given the optimization objective to maximize the TA spectral response of the PC within the band-gap zone, the objective function that is to be minimized, $E(a, w, h)$ which denoted for simplicity as $E(x)$ can be defined as

$$E(x) = \sqrt{\frac{1}{N}\sum_{\lambda=\lambda_{\min}}^{\lambda_{max}} \left(TA_{desired}(\lambda) - f_x(\lambda)\right)^2} \tag{8}$$

The discrete wavelength step size in equation (8) is based on N defined as the total number of periodic samples in the simulation process. The optimal solution can thus be found by minimizing the objective function $E(x)$, which minimizes the root mean square (RMS) error between the simulation output and the desired plateau. Moreover, an alternative objective function that can also be used to maximize emission is the emitter efficiency function (x) defined as

$$\xi(x) = \frac{\sum_{\lambda_1}^{\lambda_2} TA(\lambda)\, N_E(\lambda)}{\sum_{\lambda_{\min}}^{\lambda_{max}} TA(\lambda) N_E(\lambda)} \tag{9}$$

while $N_E(\ )$ [34,36] is defined as

$$N_E(\lambda) = \frac{2\pi c^2 h}{\lambda^5 \left(e^{\frac{hc}{\lambda k T}} - 1 \right)} \quad (10)$$

where c is the speed of light, K is Boltzmann's constant, h is the Plank's constant and T is the emitter temperature in Kelvin. While both functions can be used to identify the optimal PC geometry that achieves the desired plateau, our preliminary investigations showed that they can yield different results because the form of the objective function influences the features, contours and shape of the fitness landscape. The emitter efficiency function (Eqns. 9 and 10) proved to be more sensitive than the error function (Eqn. 8) due to the fact that small changes in the TA profiles will result in significant changes in (x) compared with $E(x)$. Therefore, the RMS error objective function (Eqn. 8) manifests a smooth landscape. On the other hand, the efficiency function, being sensitive, manifests a landscape that has sharp features and amplifies small changes in fitness when compared with the RMS error. Such a difference can be exploited to our advantage as explained in section 4.3.

4.4.3 Constraints and Variable Granularity

To produce a photonic crystal design that can successfully be fabricated, several constraints must be employed in the optimization process. Such constraints include the minimum and maximum possible thickness and width dimensions of the Lincoln-log rods that can be practically produced. We also ensure some other inequality constraints necessary to ensure that practical aspect ratios of the rod dimensions versus lattice constant is maintained. Such inequality constraints are problem specific, some defined by common sense and geometric considerations and some specified as fabrication constraints that are defined by experts [37].
In general, for the Lincoln-log crystal, we could define the following set of constraints.

$$a_{min} \quad a \quad a_{max} \quad (11)$$

$$_{w1} \cdot a \quad w \quad min(\ _{w2} \cdot a,\ a - k_1) \text{ for some constant } k_1. \quad (12)$$

$$h_{min} \quad h \quad min(\ _{h} \cdot a,\ a\text{-}k_2) \text{ for some constant } k_2. \quad (13)$$

where a_{max} and a_{min} are the maximum and minimum values of lattice constant due to fabrication process, $_{w1}$ and $_{w2}$ are the physical constraint factors for w, $_{h}$ is the physical constraint factor for h, and h_{min} is the minimal value of h due to fabrication process.

Along with the constraints on the extrema of the parameter space imposed by material properties and fabrication needs, the granularity of the design variables is also an important factor that needs to be controlled during optimization. Although simulations using RCWA can produce spectra for any real numbered values of design variables, such results would be meaningless as fabrication capabilities are limited. This 'minimum step', of the variable space, (a, w, h, l), forces a discretization of the variable space to a granularity of around 0.1 micrometer (100 nanometer). Hence we restrict the optimization process to propose solutions that are at least 100 nanometers apart. Since the spectral responses do not vary chaotically within such small steps, this enables rejecting solutions within such limited granularity.

4.4.4 Optimization Method

In this section, we propose a guided optimization technique, a hybrid methodology that uses a combination of both gradient based [41, 46, 47] and gradient-free optimization techniques [48] . Developed specifically for smart design of PC pixels with wide absorption spectrum, we explain how the proposed method differs from classical optimization techniques as well as from conventional genetic algorithms. We demonstrate how the modified search method enhances computational efficiency and convergence [49, 50].

The proposed guided semi-natural genetic algorithm can be broken down into four major steps:

Step 1: Evaluate the objective function for a few educated guesses, subject to fabrication and physical constraints based on *a priori* knowledge and domain expertise.

Step 2: Use gradient based minimization of the RMS error objective function (Eqn. 8) to improve the estimates from Step 1 to obtain solution candidates that fall in the neighborhood of optimal solutions.

Step 3: If the candidate solutions do not sufficiently meet design criteria, use these candidates as starting points to seed or "guide" a genetic optimization. At this stage switch to maximization of the emitter efficiency functions Eqns. 9 and 10 instead of RMS error minimization Eqn. 8.

Step 4: In the mutation step of the genetic algorithm, replace some of the random mutations with "unnatural" candidate solutions fed by local heuristic search.

Since gradient based optimization quickly converges on local minima we obtain a quick improvement from our initial educated guesses in step 2 of the proposed method. Gradient based techniques well perform on smooth landscapes and therefore using the RMS error objective function at this stage is beneficial. If we started with a good guess, the change to meet the performance criteria quickly is reasonably high. Otherwise, proceeding to step 3, unlike a typical GA that seeds its initial population randomly, we "guide" the GA by providing a set of individuals with a high fitness probability in the first place. This guarantees being close to the desired solution. This region is riddled with several local minima and several non-linearities and therefore is much suitable for GA rather than gradient-based optimization.

As evolutionary algorithms are not sensitive to steep slopes in the neighborhood of candidate solutions as opposed to derivative based methods, it is preferred to use a sensitive objective function and switch to the maximization of emitter efficiency (Eqn. 9 and 10). We are now interested in the local maxima that was missed in step 2, perhaps located between local extrema reachable by gradient methods. Typically, there are significantly steep ridges in the fitness landscape observed in the neighborhood of optimal solutions. At this point the genetic crossover operator provides a way of avoiding the trap of the local extrema and increases the chance of finding an alternate solution that improves the fitness of the solutions. Without the previous gradient optimization step, this event of solution candidates landing in neighboring extrema would rely purely on chance and thus can be very computationally expensive.

To reduce computation time at the mutation step of GA, we selectively replace some of the "natural" random mutations with local search, hence the term "semi-natural" off springs. Recently, researchers reported similar GA's termed "Hybrid Genetic Algorithms" or "Memetic

Algorithms" [51, 52] that were guided by heuristic search. These methods have been shown to outperform traditional GA's in certain problem domains specially when modeling time is significant.

4.4.5 Heuristic Local Search using Sliding Window

Our improvement to the GA optimization process is based on interfering in the mutation process using a heuristic search method that is based on physics-based intuitions and *a priori* knowledge. Based on empirical observations of the PC simulation process, an informal rule of thumb is that the lattice constant (a) is numerically close to the bandedge wavelength (the end of the bandgap). Moreover, changes in width and height of PC seem to be linearly related to lattice constant change, over narrow variation range. By observing the bandgap region in the neighborhood of the desired plateau, it was obvious that there exists a lattice constant candidate that can lead to a TA plateau considerably close to the desired plateau. If such a candidate solution is found a significant computational saving can be achieved compared with the purely natural evolving solution using genetic algorithm.

To exploit this fact, we implemented a sliding window function that computes the emitter efficiency not just at the desired bandgap but for a series of bandgaps ranging from $-1.5\ _W$ to $1.5\ _W$ of the desired bandgap with $_W$ being the bandedge as shown in Figure 4.11. If the value of the objective function (Eqn. 9) for the sliding window ($_2$) is greater than the value of the objective function at the desired bandgap ($_1$), a new heuristically inspired candidate PC geometry, $x_n = \langle a_n, w_n, h_n \rangle$, is computed considering $x_n = k\, x_0$, where $x_0 = \langle a_0, w_0, h_0 \rangle$ represents the original PC geometry and $k = (\ _2)/(\ _1)$, corresponds to the ratio between the desired and detected bandedges.

The relative expected improvement in fitness, $= (\ _2 - \ _1)/\ _2$, is used as a stochastic parameter to decide whether the physics-based candidate identified by the sliding window search is to be included in the next generation as a replacement of a candidate determined by the "natural" mutation or not. A threshold value for needs to be set such that the improvement is beyond typical variations in the objective function due to noise.

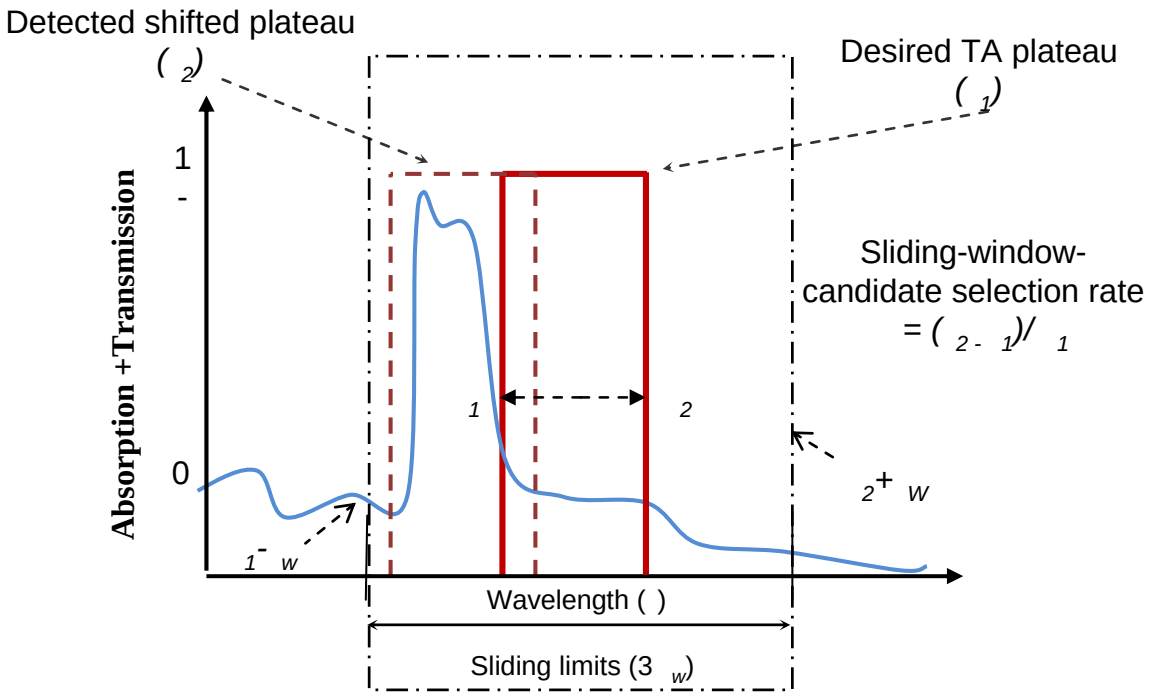

Figure 4.11 The sliding window heuristic and the selection rate depending on expected improvement in efficiency.

4.4.6 Spectral Caching

Finally, one of the main obstacles in optimization of photonic crystals is the computationally expensive methods used to compute the photonic spectral response of a crystal given the PC geometry. Typically, on a 2 GHz dual processor with 1 GB desktop machine running the RCWA simulation described above, computing each point on the spectra takes about 40 seconds. Therefore, computing the 120 or so points needed for establishing the entire spectrum such that either of the objective functions can be evaluated once required about 1.5 hours. If classical GA is used, each generation includes 20 individuals; the computation of one generation will take about 30 hours. If GA is to converge to the desired PC geometry in 5 to 7 generations, simulations worth one week are required. This might be reduced to two days if the simulations are carried out on an eight node parallel processor. The above details about computation time are necessary to realize the computational expenses of the problem at hand.

However, it is worth noting that the TA spectrum for a given PC geometry is a physical property and is invariant with respect to the region of bandgap of interest and the objective

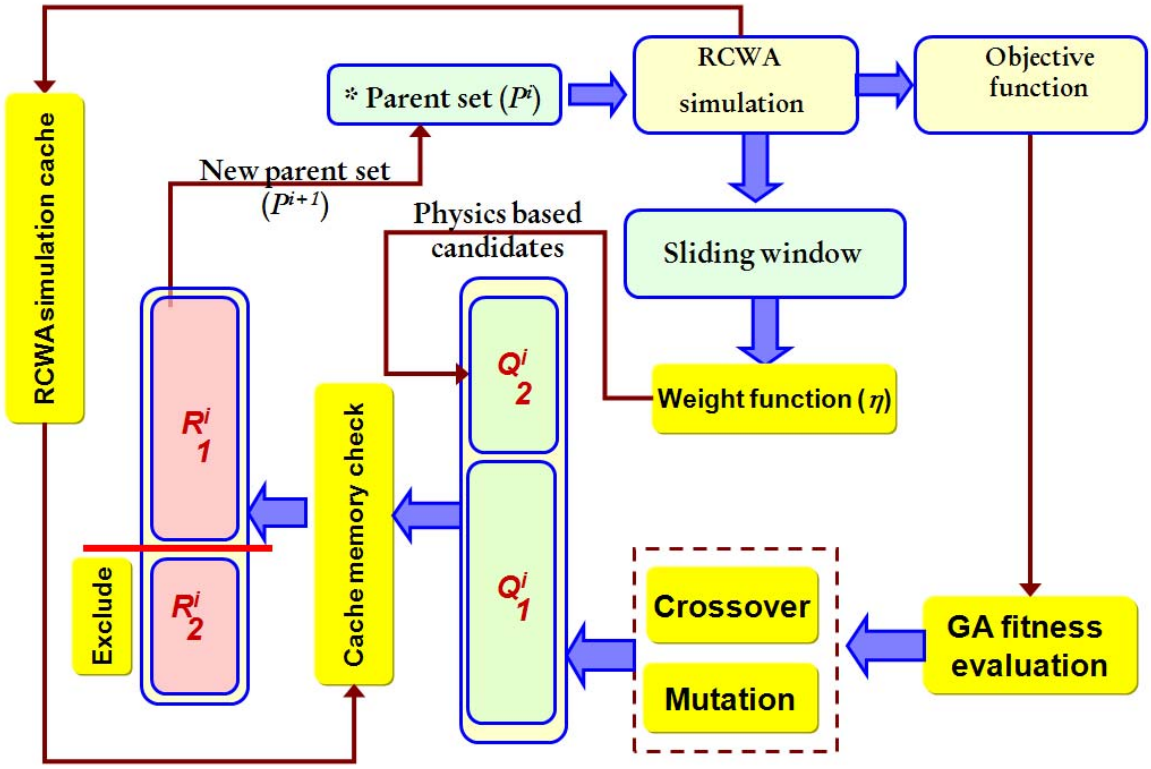

Figure 4.12: The proposed semi-natural GA including the different components.

(* indicates the starting point on the optimization)

function(s) under consideration. This means some of the computations used in optimizing pixel # 1 can be used as pivotal points for optimizing pixel #2. Pivotal points could be starting points, points used in the evolutionary process or points in the neighborhood that could help in quick computation of the objective function gradient. Furthermore, we also realize that in a GA optimization, a number of the individuals in the new population would typically have already existed in previous populations as a result of implementing principles of elitism or due to multiple-crossovers [47]. Therefore, there is a significant chance that the simulation process will be repeated during a few consecutive generations in GA. We immediately realize the utility of tabulating and caching the results of each simulation run, storing them away into secondary storage.

We therefore implement a spectral caching technique. While this process is less useful when searching in a bandgap region never searched before, it becomes increasingly useful in successive searches in the neighborhood, making the need for new simulations rare. Figure 4.12 presents a schematic describing the above explained (semi-natural) genetic optimization process. Figure 4.12 also shows how the spectral caching and the heuristic search methods are used to interfere in the evolution process. It can also be observed in Figure 4.12 that, in each optimization run, the new individuals Q_1^i created using natural GA crossover and mutate is

mixed with the group of individuals denoted Q_2^i who were promoted from the sliding window heuristic search as physics based candidates yielding a new pool of individuals ($Q_1^i + Q_2^i$). The new pool of individuals is checked against the previously cached solutions. The new pool of individuals are thus divided into two groups. First, the new generation solutions R_1^i that have never been simulated before and is used for forming the new parent set P^{i+1}. Second, a group of solutions that have already been cached R_2^i which is excluded from the new optimization run. We claim that such interference in the evolution process using the sliding window and the memory caching techniques results in significant time savings in the optimization process.

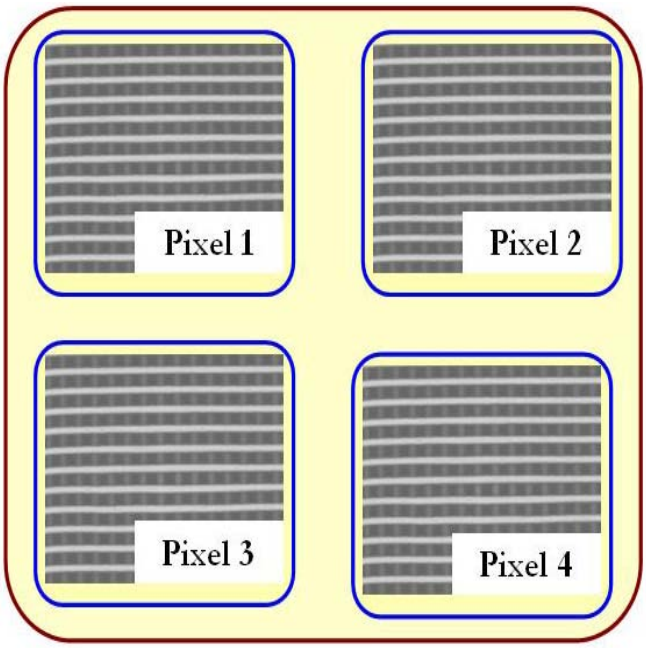

Figure 4.13: Schematic representation of photonic crystals used to create a multi-pixel system as per case study.

4.4.7 Case Study

Here we present one case study for multi-pixel optimization and we demonstrate the ability of the proposed method to provide an independent optimal PC structure at each pixel that satisfies a predefined spectrum such that the four pixels cover the whole spectrum of interest. The predefined absorption and transmission spectra for the four pixels are (3.45-4.45 μm) for pixel 1, (4.00-4.8 μm) for pixel 2, (8.15-9.55 μm) for pixel 3 and (10.0-11.5 μm) for pixel 4. The four pixels are shown schematically in Figure 4.13. The required PC in the four pixels is assumed to be an 8 layer PC with the following fabrication constraints.

In the next section we present the results for this optimization process. We show that using a gradient optimization guided GA with semi-natural evolution enhances the ability of the proposed method to reach design solutions not attainable using traditional GA optimization and to reach such solutions at computational time much less than non-guided GA.

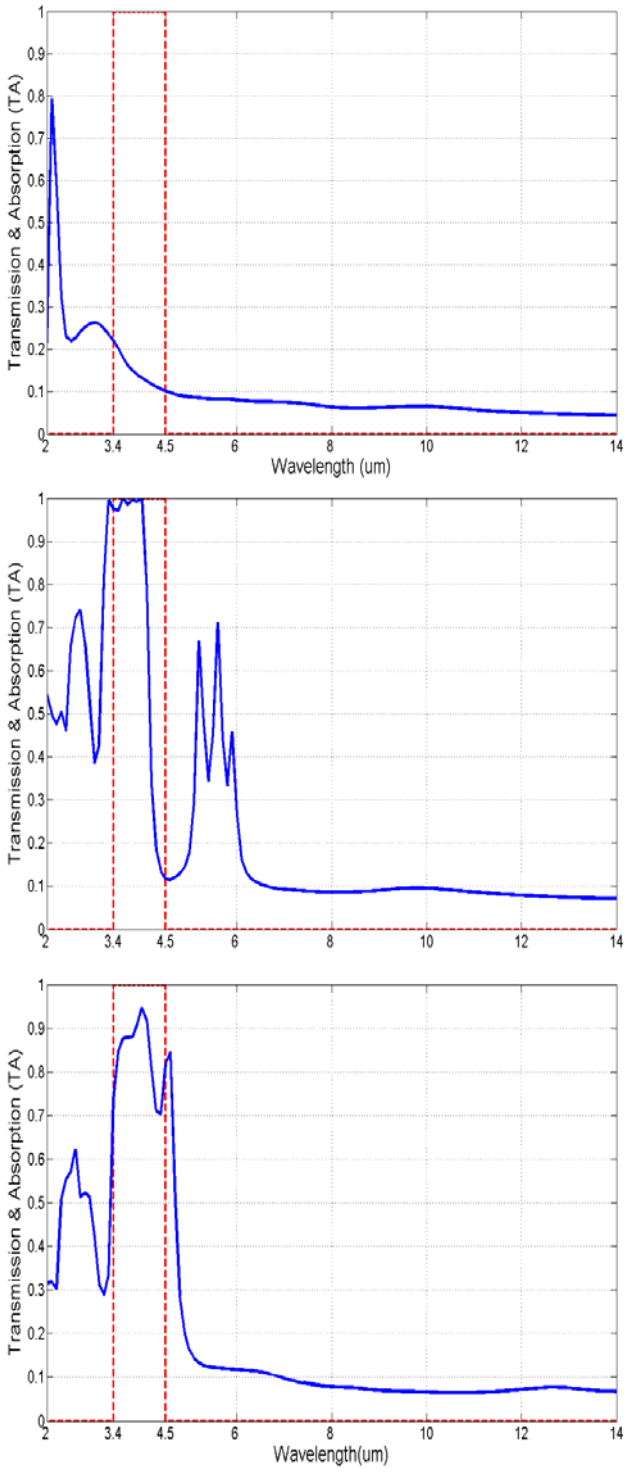

Figure 4.14: TA Optimization in Pixel 1. (a) design 1, (b) design 2 and (c) design 3. optimal Spectral response achieved for a PC geometry (design 3) of lattice constant (a) = *3.4 m*, rod width(w) = *0.7 m*, height(h) = *0.8 m*

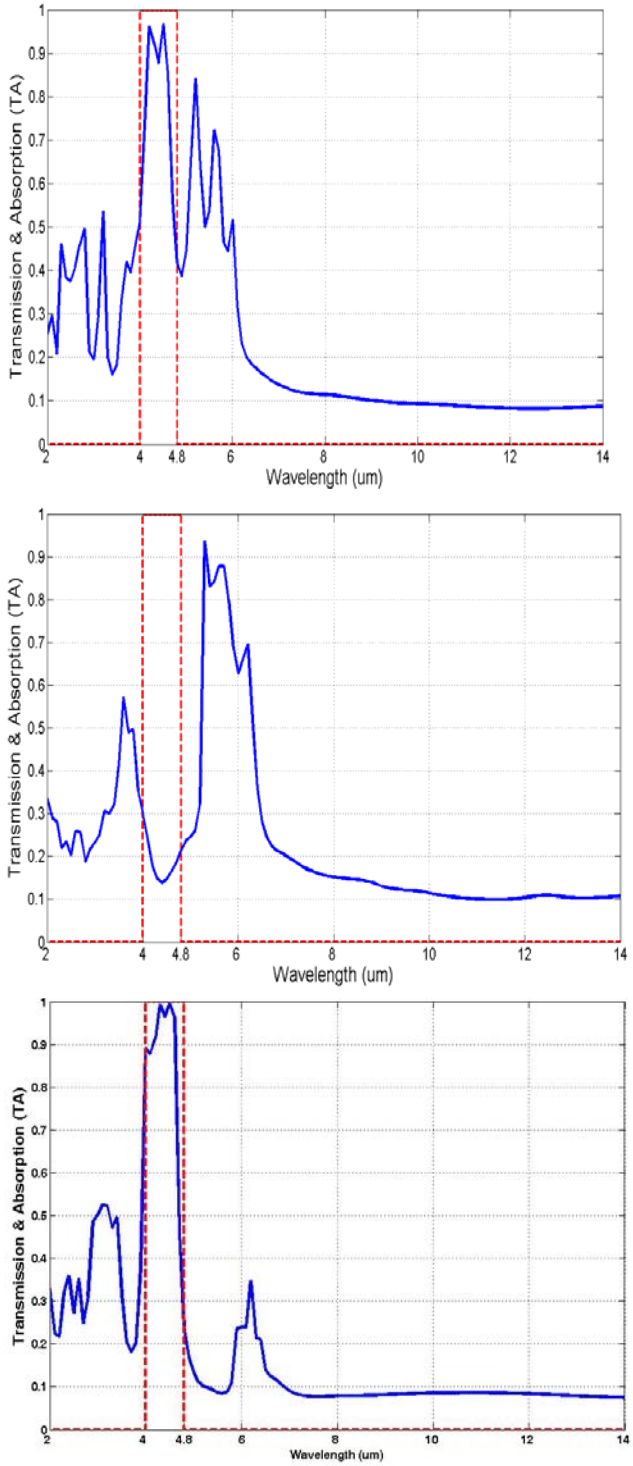

Figure 4.15: TA Optimization in Pixel 2. (a) design 1, (b) design 2 and (c) design 3. optimal Spectral response achieved for a PC geometry (design 3) of lattice constant(a) = *3.9 m*, rod width(w) = *1.3 m*, height(h) = *2.0 m*

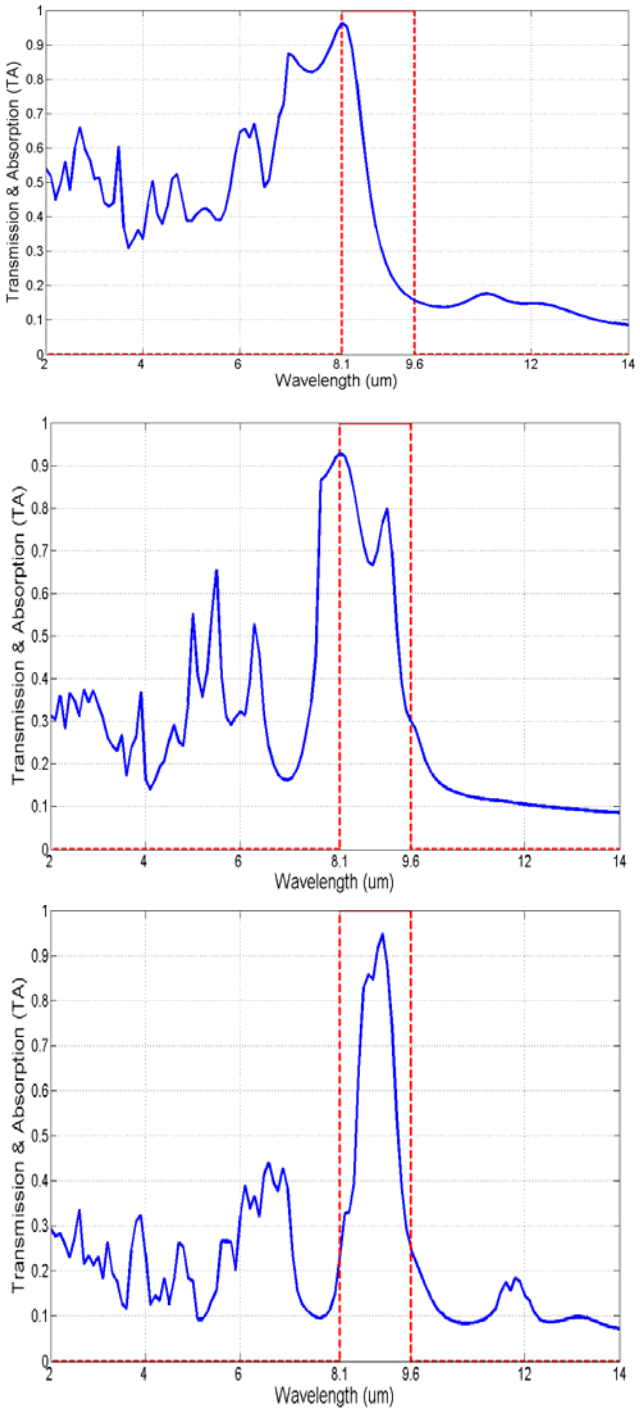

Figure 4.16: TA Optimization in Pixel 3. (a)design 1, (b) design 2 and (c) design 3. optimal Spectral response achieved for a PC geometry (design 3) of lattice constant(a) = *8.4 m*, rod width(w) = *3.4 m*, height(h) = *4.2 m*

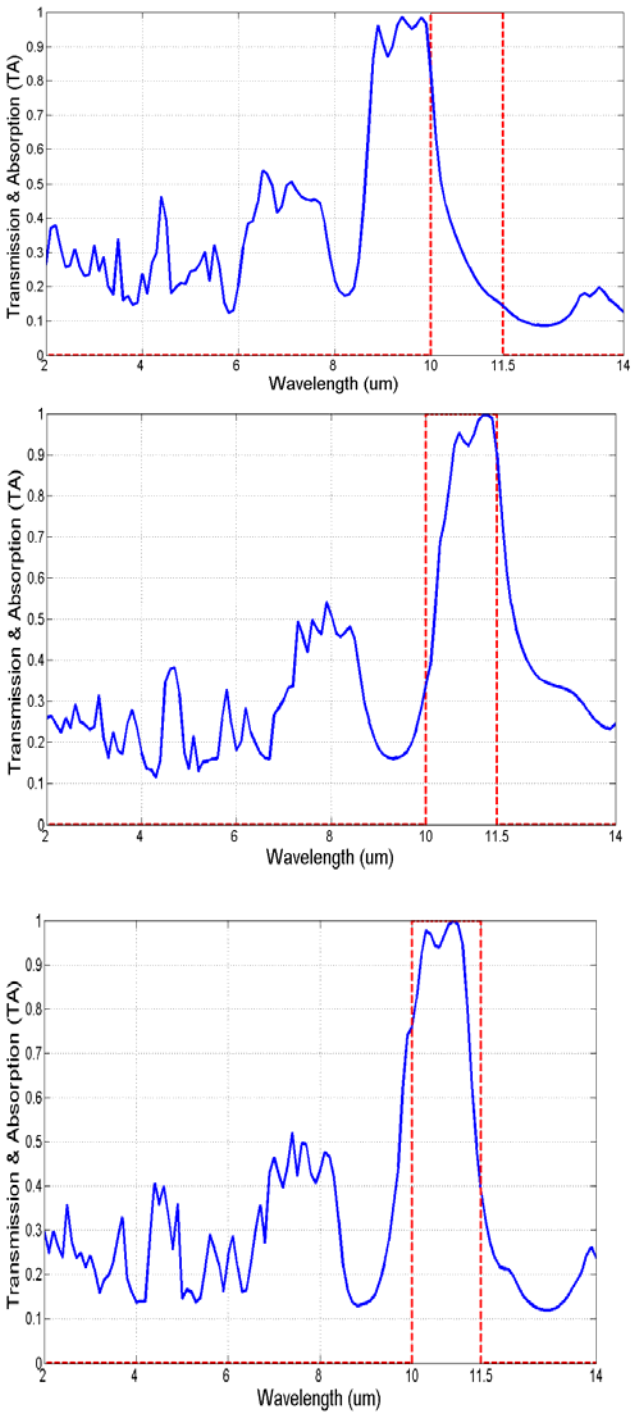

Figure 4.17**:** TA Optimization in Pixel 4. (a) design 1, (b) design 2 and (c) design 3. optimal Spectral response achieved for a PC geometry (design 3) of lattice constant(a) = 9.*8 m*, rod width(w) = *3.4 m*, height(h) = *4.8 m*

4.5 Results and Discussions

In this section we report the quality of the design solutions achieved for the four pixels in the multi-pixel photonic system described in the previous section. The final emitter efficiency is computed using Eqns. (9) and (10). Pixel 1 is intended to operate in the (3.45 - 4.45 μm) wavelength range. In Figure 4.9, we show the evolution of the solution showing various exemplary stages of the optimization process. Figure 4.14(a) shows how the gradient descent technique terminated in an undesirable local extrema. The design that produced the response in Figure 4.14(b) showed up at the genetic optimization stage, which underwent a modification of design by the sliding window local search heuristic to yield the response shown in Figure 4.14 (c), the final design that achieves an emitter efficiency of 53.9% at 712K.

With Pixel 2, gradient descent proved more successful (Figure 4.15 (a)) than with Pixel 1 and was able to provide a good starting point for the semi-natural genetic optimization which produced the designs shown in Figure 4.15 (b) and 4.15 (c) respectively. Figure 4.15 (c) is the final solution which achieves an emitter efficiency of 44.3% at 646K for the desired wavelength region.

Moreover, Pixel 3, the gradient descent provided a solution, as shown in Figure 4.16 (a), that seemed little be towards the higher wavelength region, it was also observed to have a lot of high emission in the undesired lower wavelength regions. The semi-natural genetic optimization process provided the successive solutions shown in Figure 4.16 (b) and 4.16 (c) resulting in an emitter efficiency of 50.9 at 256 K.

Table 4.1**:** Emitter efficiency of Pixels 1, 2, 3 and 4 at zero angle of incidence using optimal PC configurations and peak efficiency temperatures.

Pixel	Lattice constant (a) m	Rod width (r) m	Rod height (h) m	Emitter efficiency %	Peak efficiency temperature (^{o}K)
Pixel 1	3.4	0.7	0.8	*53.9*	712
Pixel 2	3.9	1.3	2.0	*44.3*	646
Pixel 3	8.4	3.4	4.2	*50.9*	256
Pixel 4	9.8	3.4	4.8	*54.5*	169

Finally Pixel 4 represents the most challenging design among the four pixels due to the well- known low emissivity of Tungsten for long wavelengths (10 – 11.5μm). Although in this case, gradient descent method did not provide initial good designs, Figure 4.17 (a) shows a candidate “slide-able” solution that appeared in the genetic optimization process. With the application of the local search heuristic approach using the sliding window technique to replace some of the “natural” mutations (Figure 4.17 (b)), a surprisingly high emitter efficiency of 54.5% at 169 K can be achieved, as shown in Figure 4.17 (c). A summary of emitter efficiency for the four optimized PC pixels at zero angle of incidence (α) using optimal PC configurations are presented in Table 4.1. The temperatures reported in Table 4.1 are those temperatures where

efficiency peaks occurred. The relationship between the temperature and candidate design solutions and the emitter efficiency for Pixel 2 is shown as an exemplar relation in Figure 4.18.

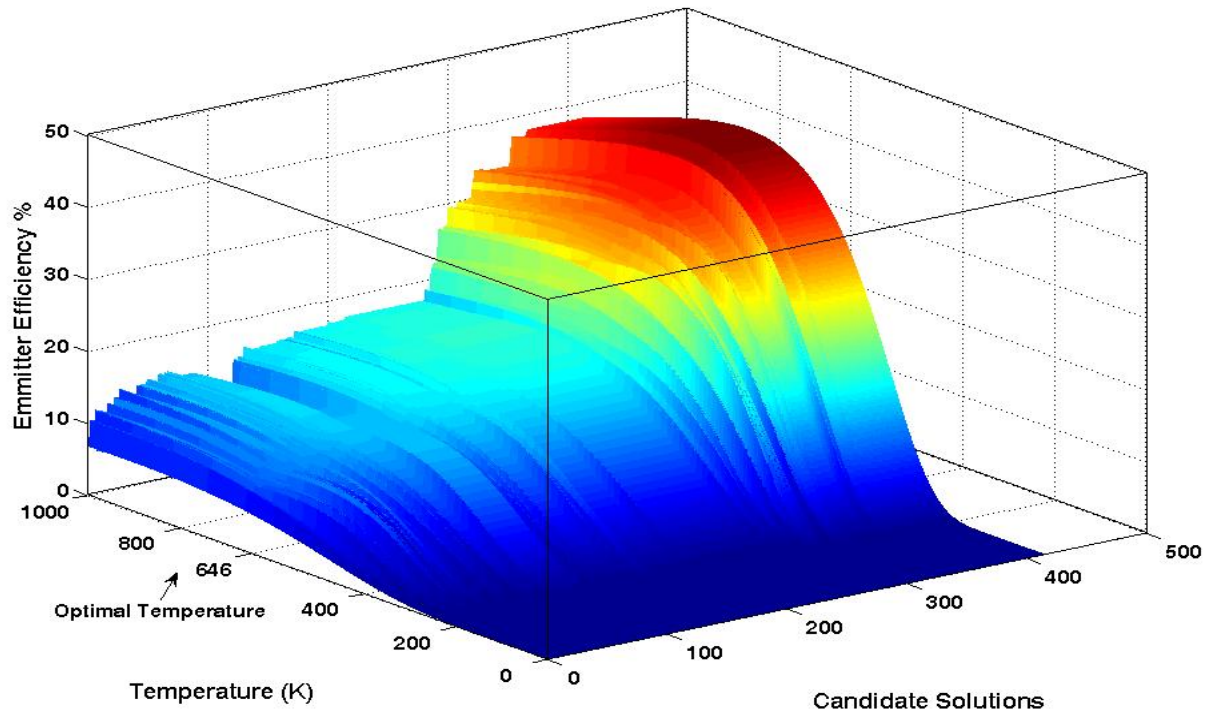

Figure 4.18: Relationship between Temperature (K) of individual design solutions for Pixel 2. considered by GA during the evolution process and the emitter efficiency showing the optimal design to have the peak efficiency at 646 K.

Figure 4.19 (a) shows that the quality of solution (high emitter efficiency %) that was reached by gradient descent method was not as high as the solutions reached by genetic optimization or guided genetic optimization. Figure 4.19(b) shows that guiding the genetic optimization process through a semi-natural mutation shows a reduction in the total number of iterations necessary to find the optimal solution. Figure 4.19(b) also shows that the sliding window heuristic further reduces the number of iterations required for convergence.

Finally, considering Figure 4.19(c), while a similar trend for reducing running time for techniques 1 through 4 can be observed, it is worth noting that using technique 5 that employs the spectral caching technique shows a significant reduction in effective running time of the entire optimization process compared to all other methods.

The above proposed method and discussion demonstrate the fact that artificial intelligence (AI) –based techniques can provide smart design methods for complex design problems where the traditional iterative process of trial and error proved to be inefficient and computationally very expensive. We also showed that an approach where AI-based techniques (here GA) is interwoven with heuristic methods that is established using physics principles driven from problem specifics can result in significantly enhancing the design process and design solutions compared with direct application of existing AI-based techniques. Finally, for future

explorations, we expect to evaluate and improve this technique for other PC geometry types, like hexagonal, face-centered cubic and aperiodic structures. Work on parallelization of the technique and evaluation on a distributed computing system is also under way.

4.6 Conclusions

We conclude stating that while the general problem of PC design is intrinsically challenging, the proposed semi-natural GA method enabled the successful design of a challenging multi-pixel PC system while also reducing the average computing time taken per design. In addition, our methods allowed for the realization of PC designs that resulted in an average emitter efficiency of ~50% over a wide range of infrared wavelengths. We specially note the unprecedented high emitter efficiency of 55% at a significantly long wavelength region. To put this in perspective, average non-photonic crystal thermal emitter efficiencies reside below 40%, and the highest reported PC efficiency in the literature was reported to be around 40% [53].

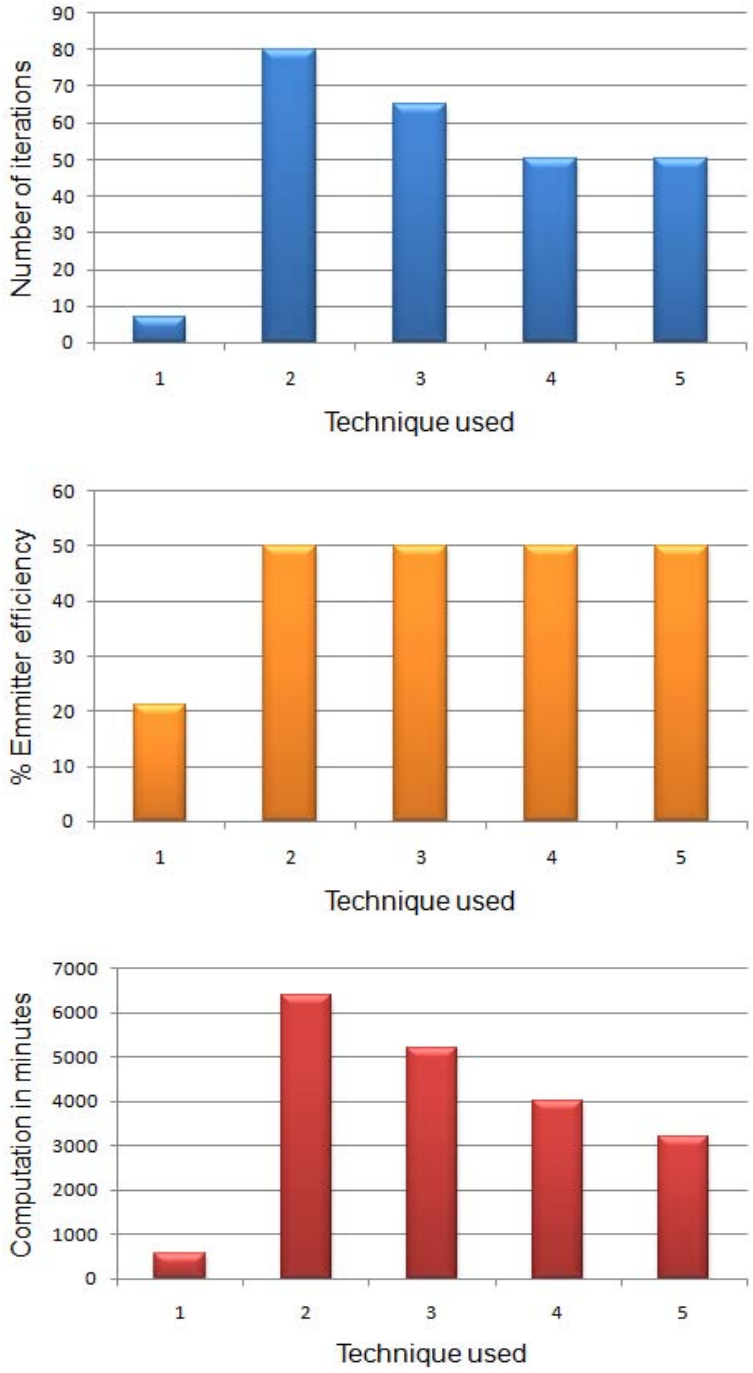

Figure 4.19: A comparison of performance of the techniques used. 1. Gradient Descent (GD) 2. Genetic Algorithm (GA) 3. GD guided GA (GDGA) 4. GDGA with Sliding Window local search Heuristic (GDGASW) 5. GDGASW with Spectral Caching (GDGASWSC)
(a) Number of iterations
(b) Quality of solution
(c) Computational time

4.7 References

[1] Ross, T. J. (2004). *Fuzzy logic with Engineering applications*. Second Edition, John Wiley and Sons. UK.

[2] Akai, T. (1994). *Applied numerical methods for Engineers*, John Wiley & Sons, NY.

[3] S.Y., Lin, J. G., Fleming, D. L., Hetherington, B.K., Smith, R., Biswas, K.M., Ho, M. M., Sigalas, W., Zubrzycki, S.R., Kurtz, J. A. Bur. "Three-dimensional Photonic Crystal Operating at Infrared Wavelengths", Nature, 394: pp.251-253 (1998).

[4] Biswas, R., El-Kady, I., Lin, S.Y., Ho, K.M. "Complete Photonic Band Gap in the Optimized Planar Diamond Structure", Photonics and Nanostructures fundamentals and applications, 1(1): pp. 15-21 (2003).

[5] S.Y., Lin, J. G. Fleming, E. Chow, "Two- and three-dimensional photonic crystals built with VLSI tools", MRS Bulletin; 26: pp. 627-31 (2001)

[6] K. Robbie, M.J. Brett, and A. Lakhtakia, "Chiral Sculptured Thin Films", Nature 384, 616, (1996).

[7] J.G. Fleming, S.Y. Lin, I. El-Kady, R. Biswas, K.M. Ho. All-metallic three-dimensional photonic crystals with a large infrared bandgap. Nature, 417, 52 (2002).

[8] I. El-Kady, M.M. Sigalas, R. Biswas, K.M. Ho, C.M. Soukoulis. Metallic photonic crystals at optical wavelengths. Physical Review B, 62, 15299 (2000).

[9] M. Sigalas, C.M. Soukoulis, C.T Chan, D.Turner, Phys Rev B, 53, 8340 (1996).

[10] Su, M. F., M.Sc. Thesis, Department of Electrical and Computer Engineering, University of New Mexico, 2006.

[11] A.J. Ward and J. B. Pendry, Computer Physics Communications. 128 (3): 590-621 (2000).

[12] J.B.Pendry, Journal of Modern Optics, 41 (2): 209-229 (1994).

[13] I. El-Kady, Zhi-Yuan Li, and K.M. Ho, An analytical modal expansion method applied to 3D layer-by-layer metallic photonic crystals. Photonic and Electromagnetic Crystal Structures (PECS-IV) Conference Proceedings: Molding the flow of light on a chip, P.126 (2002).

[14] S. Y. Lin, J. G. Fleming, and I. El-Kady, "Highly efficient light emission at m5.1 = by a three-dimensional tungsten photonic crystal," Optics Letters 28(18), 1683-1685 (2003).

[15] GD-Calc™, The "Grating Diffraction Calculator", Kenneth C. Johnson, 2006.

[16] MATLAB®, The Mathworks Inc., MA, USA, 2005.

[17] Venkataraman, P., Applied Optimization with MATLAB Programming. John Wiley and Sons Inc. NY, USA, 2002.

[18] Nash, J. C. Compact numerical methods for computers: linear algebra and function minimization. Adam Hilger, 2nd Edition, 1990.

[19] Jang, J., -S., R., Sun, C., -T. and Mizutani, E. (1997). *Neuro-Fuzzy and soft computing, A computational approach to learning and machine intelligence*. 1st edition, Prentice Hall Inc., Englewood Cliffs, N.J., USA.

[20] Vanderplatts, G. (1984). *Numerical optimization techniques for engineering design with applications*. McGraw-Hill, NY, USA

[21] Coley, D. A. (1999). *An Introduction to Genetic Algorithms for Scientists and Engineers*, First Edition, 1999, World Scientific, Singapore.

[22] H. Szu and R. Hartley, Fast simulated annealing, Physics Letters A. Vol.122, No.3-4, 1987, pp: 157-162.

[23] Fletcher, R. Practical Methods for Optimization, John Wiley & Sons, NY, USA, 1980.

[24] Levenberg, K. A method for solution of certain problems in least squares. Quarterly Applied Mathematics, Vol.2, 1944, pp: 164-168.

[25] Marquardt, D. W. An algorithm for least squares estimation of nonlinear parameters. Journal of the Society of Industrial and Applied Mathematics. Vol. 11, 1963, pp: 431-441.

[26] J.Y. Fan and Y.X. Yuan, On the convergence of a new Levenberg-Marquardt method, Technical Report, AMSS, Chinese Academy of Sciences, 2001, 11p.

[27] Cordón, O., Herrera, F., Hoffmann, F. and Magdalena, L. (2001). *Genetic Fuzzy Systems: Evolutionary Tuning and Learning of Fuzzy Knowledge Bases*. World Scientific, Singapore

[28] Spears, W. M. (1993). Crossover or mutation? Whitely, L. D. Ed., *Foundations of genetic Algorithms*, Morgan Kaufmann, NY, USA.

[29] J. M. Mendel. Uncertain Rule-Based Fuzzy Logic Systems: Introduction and New Directions. (2000), First Edition, Prentice Hall, NY, USA.

[30] Shan, X., Reda Taha, M. M. and Caudell, T. "Fuzzy systems to speed GA convergence", University of New Mexico, Unpublished document.

[31] Grabisch, M., Nguyen, H.T. and Walker, E.A. (1995). Fundamentals of Uncertainty Calculi with Applications to Fuzzy Inference. Kluwer Academic.

[32] Chiang, J.H. (1999). Choquet fuzzy integral-based hierarchical networks for decision analysis. IEEE Trans. On Fuzzy Systems (7), No.1; 63-71.

[33] Johnson SG, and Joannopoulos, JD. *Photonic Crystals – The Road from Theory to Practice*. ISBN-13: 978-0-792-37609-5. Kluwer, 2002.

[34] Yablonovitch E. Inhibited Spontaneous Emission in Solid-State Physics and Electronics. *Physical Review Letters* 1987; Vol. 58, 2059

[35] Lin SY, Fleming JG and El-Kady I, Highly efficient light emission at m5.1 = by a three-dimensional tungsten photonic crystal. *Optics Letters* 2003; 28(18), 1683-1685.

[36] Lin SY, Fleming JG and El-Kady I, Three-dimensional photonic-crystal emission through thermal excitation. *Optics Letters* 2003; 28, 1909-1911.

[37] Lin SY, Moreno J and Fleming JG, Three-dimensional photonic-crystal emitter for thermal photovoltaic power generation. *Applied Physics Letters*, 2003, 83 (2), 38—382.

[38] Glytsis EN and Gaylord TK, Rigorous three-dimensional coupled-wave diffraction analysis of single and cascaded anisotropic gratings. *J. Optical Society of America A.*, 1987; 4: 2061-2080.

[39] Venkataraman, P., *Applied Optimization with MATLAB Programming*. John Wiley and Sons Inc. NY, USA, 2002.

[40] Taflove, A and Hagness SC, Computational Electromagentics: The Finite Difference Time Domain Method. Boston, MA: Artech House, Second Ed., 2000.

[41] Davidovich, MV, Green functions and integral equations for photonic crystals. *Microwaves, Radar and Wireless Communications, MIKON-2004. 15th International Conference*, Vol. 2, Issue , pp. 597 – 602, (2004)

[42] Pendry, JB, Photonic band structures, *Journal of Modern Optics*, 1994, 41 (2): 209-229.

[43] Li, L, Formulation and comparison of two recursive matrix algorithms for modeling layered diffraction gratings. *J. Optical Society of America A.*, 1996, 13 (5): 1024-1035.

[44] Chateau N, Hugonin, JP, Algorithm for the rigorous coupled-wave analysis of grating diffraction, *J. Optical Society of America A.*, 1994, 11(4): 1321-1331.

[45] Levenberg K. A method for solution of certain problems in least squares. *Quarterly Applied Mathematics*. 1944; 2: 164-168

[46] Marquardt DW. An algorithm for least squares estimation of nonlinear parameters. *Journal of the Society of Industrial and Applied Mathematics.* 1963; 11: 431-441.

[47] Coley DA. *An Introduction to Genetic Algorithms for Scientists and Engineers*, *First Edition*, World Scientific, Singapore, 1999.

[48] Fan JY and Yuan YX, On the convergence of a new Levenberg-Marquardt method, Technical Report, *AMSS, Chinese Academy of Sciences*, 2001, 11p.

[49] Rudolph G. Convergence of evolutionary algorithms in general search spaces. *Third IEEE Conference on Evolutionary Computation*, 1996, pp: 50-54.

[50] Krasnogor N and Smith J. A Tutorial for Competent Memetic Algorithms: Model, Taxonomy, and Design Issues, *IEEE Transactions on Evolutionary Computation*, 2005; 9 (5): 474- 488.

[51] Il-Seok Oh, Jin-Seon Lee, Byung-Ro Moon, Hybrid Genetic Algorithms for Feature Selection. *IEEE Transactions on Pattern Analysis and Machine Intelligence*, 2004; 26 (11): 1424-1437.

[52] Fleming, JG, Lin, SY, El-Kady, I, Biswas, R and Ho, KM "All-metallic three-dimensional photonic crystals with a large infrared bandgap", *Nature*, 2002, 417, 52-55.

5. Novel structures: Three Dimensional BCC Chiral Photonic Crystals Fabricated by Deep X-ray Lithography

5.1 Background

We have designed a novel fabrication scheme for a photonic crystal structure that produces a large area 3-D chiral band gap for either left or right circularly polarized light but not both. The opposite polarization transmits through the material without appreciable reflection. Thus, such a structure can be used for a variety of chiral detection schemes including but not limited to tag track and locate applications, dichroic spectroscopy, and Faraday rotation of light in very thin films without large external electric or magnetic fields.

Several attempts have been made to generate chiral photonic crystals since it was first proposed by Toader and John in 2001 [1]. The simplest examples are 2-D arrays of polymer spirals pointing up out of the plane [2,3,4]. These structures clearly demonstrate a 1-D bandgap for left vs. right circularly polarized light at normal incidence. These devices are fabricated using multi-photon and holographic lithography to generate spiral resist patterns in close proximity to one another but not intertwined. Unfortunately there is a symmetry break along the <110> axis of these structures that prevents the formation of a uniform 3-D band gap. Other attempts include fabrication of an intertwined 3-D chiral crystal using Glancing Angle Laser Assisted Deposition (GLAD) [5,6,7]. The device was fabricated in a serial process requiring a laser to be stitched periodically across the entire field to initiate metal deposition and grow the crystal up from the substrate a few nm at a time. Early attempts to establish the process resulted in connected coils. This reduced the band gap to that of a 2-D photonic structure [5.6]. Recent improvements in GLAD processing have allowed for the demonstration of unconnected entwined structures over a 40 mm^2 area. However the process has only been demonstrated using with a simple cubic lattice structure.

The current design creates a body centered cubic (BCC) crystal symmetry by moving the coils even closer so that they spiral between one another as shown in Figure 5.1. Although the coils themselves never touch, neighboring structures interweave out of plane with each other to increase the total density and symmetry of the device. Figure 5.2 illustrates a single set of spiral structures similar to those envisioned for this device. The figure shows multiple interweaved loops of material suspended either in air or in a transparent media covering the substrate. The device shown in Figure 5.1 is an assembly of 4 such patterns connected at specific locations to produce a BCC unit cell. Unlike previously demonstrated chiral PBG's this structure maintains

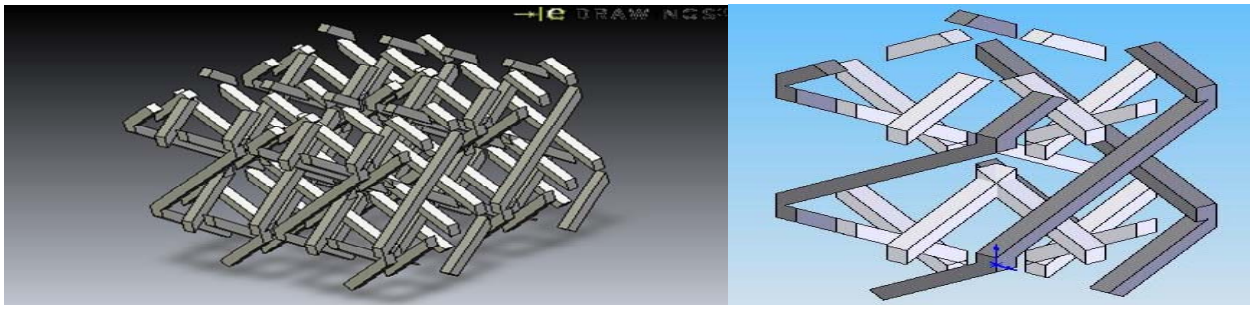

Figure 5.1: 3D nested chiral photonic crystal

the same observable distances between neighboring beams from all orientations, thereby demonstrating the improved symmetry required to for a wide band gap material photonic band gap from any incidence angle for only 1 type of circular polarization and not the other.

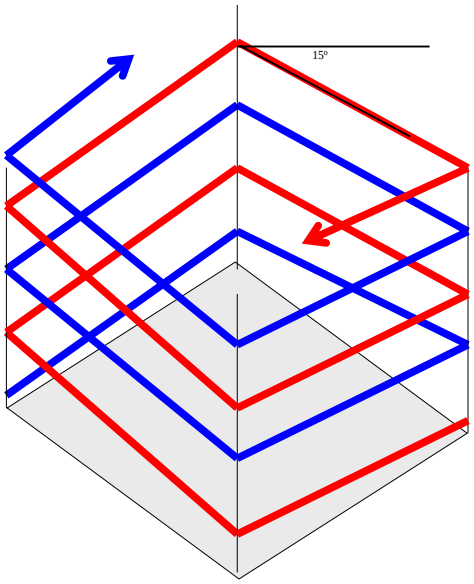

Figure 5.2: Single section of spiral structure envisioned in for the 3-D chiral PBG

5.2 Device Applications

Light impinging on the structure will be reflected or transmitted within the band gap as described below:

- **Used for Tag Track and Locate applications**
- **Used in transmission**, a chiral film could rotate the polarization vector of any IR input. This film acts like an extremely thin Faraday rotator where any polarization can be the rotated by some pre-selected angle between $\pm 90^{o}$. This component could be extremely useful in optical signal processing or emission modification.
- **Used for dichroic spectroscopy,** these devices could be fabricated at a number of different wavelengths currently used to measure spectroscopic data from large biological molecules and explosive materials. Many of these materials have chiral symmetries with similar molecules that function in a very different manner. The ability to analyze the products during chemical manufacturing steps, provide onside detection of explosives, and examine the working nature of different protein complexes will have a significant impact on the future of these fields. This technique is currently used in both the IR and THz wavelengths. However, it requires a large number of optical components that can be greatly reduced by using a single transmissive chiral PBG and detector configuration. Three dimensional crystals not only provide this, but they also allow for field use where samples may not illuminate the crystal from a single orientation, but from any number of different angles of incidence.

The functionality of this structure allows for a number of different highly desirable application spaces. Any one of these uses can be applied directly to basic science and/or national security applications.

5.3 Fabrication Methodology

For infrared applications, we envision creating this structure using conventional Deep X-ray Lithography (DXRL) techniques to pattern large areas of negative photoresist that will be used as a mold for depositing the metal structure. This technique allows for the production of a BCC chiral crystal with band edges between 8 and 100 μm over areas up to 400 mm^2 in any number of different electroformed metals and alloys. A more complex DXRL solution of other lithographic means can be used for shorter wavelengths. Two different geometrical patterning variations were developed for producing the basic coil design in this device. Additional exposures performed after these steps isolate each coil and prevent electrodeposition in regions that would otherwise prevent success.

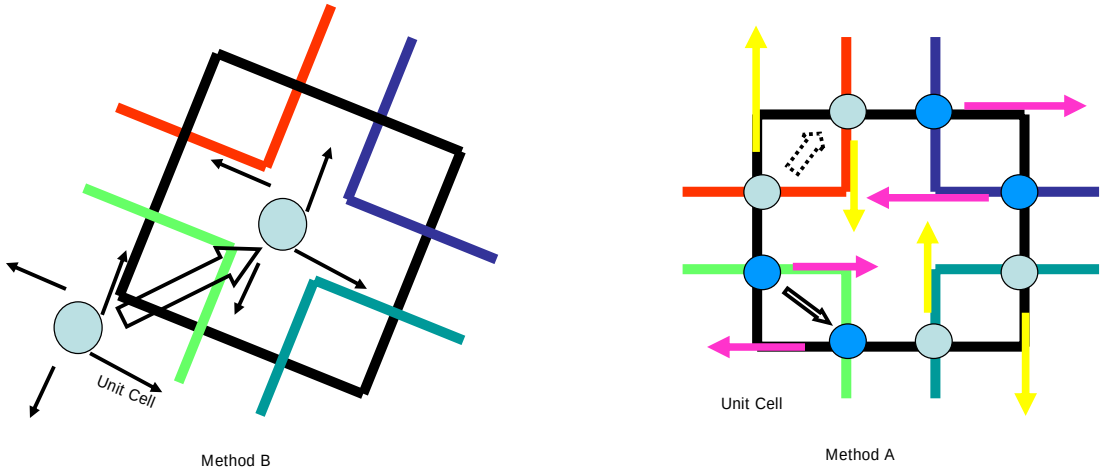

Figure 5.3: Two different methods for manufacturing chiral patterns in resist.

Figure 5.3 illustrates each of the patterning methods. The pattern is exposed at a 12.5 degree angle into the resist. Method A, is the optimal manufacturing design demonstrating the proper physical properties. Two different masks are used to create the various coil geometries in the resist. Mask one is represented by grey-blue circles in the diagram. Mask 2 is represented by the dark blue circles. Each solid arrow in the feature represents a particular exposure pattern printed in the resist. The yellow arrows represent exposed patterns using mask 1. It should be noted that the yellow arrows are oriented in two different directions. First the mask and substrate are tilted at 75 degrees off normal to the light source and exposed to pattern the resist at a 15 degree angle from grazing. Then the mask is shifted over with respect to the substrate by a small distance. This is represented by the black dash arrow between the closest yellow arrows. The mask and substrate are then clamped again and rotated about the normal by 180 degrees. The mask and substrate are then tilted again to 75 degrees and exposed. Together these exposures generate two sides of every coil in the structure. Next, a second mask is aligned and exposed in a similar manner but at right angles about the normal axis to the structures indicated by the yellow arrows. The pink arrows indicate exposures using mask 2. The black arrow represents movement second mask between exposures of arrows oriented in different directions. In total there are 4 exposures required to generate all of the patterns necessary to produce a connected coil structure.

An alternate fabrication scheme for producing connected coils is illustrated as method B. This scheme uses a single mask expose the resist in four different orientations. Each orientation is represented by a black arrow in the pattern. They are all exposed so that the resist is crosslinked at an elevation angle of 15 degrees from the resist surface. Furthermore all exposures are at right angles with respect to one another. The mask is then shifted parallel to the surface diagonally by 0.707 of the unit cell and exposed again to generate the remaining patterns required to create the connected coil structure.

Note that there is an additional rotational offset in the Method B design. This additional in plane rotation is used in conjunction with a predefined gap distance between the mask and substrate based on the periodicity and thickness of the chiral PBG to generate resist patterns that do not line up directly with their nearest neighbors. Instead they are shifted over by approximately 1 beam width. This team has previously demonstrated the effectiveness of such a rotation to create an out of plane tilted logpile photonic crystal. [8]. This method reduces the number of masks and alignment steps required to complete the structure. However, it does require the production of a slight tetrahedral shape in the lattice structure. This technique may not be suitable for very thick crystals, but may provide sufficient band gaps to demonstrate 1-3 unit cell thick structures with fewer alignment considerations.

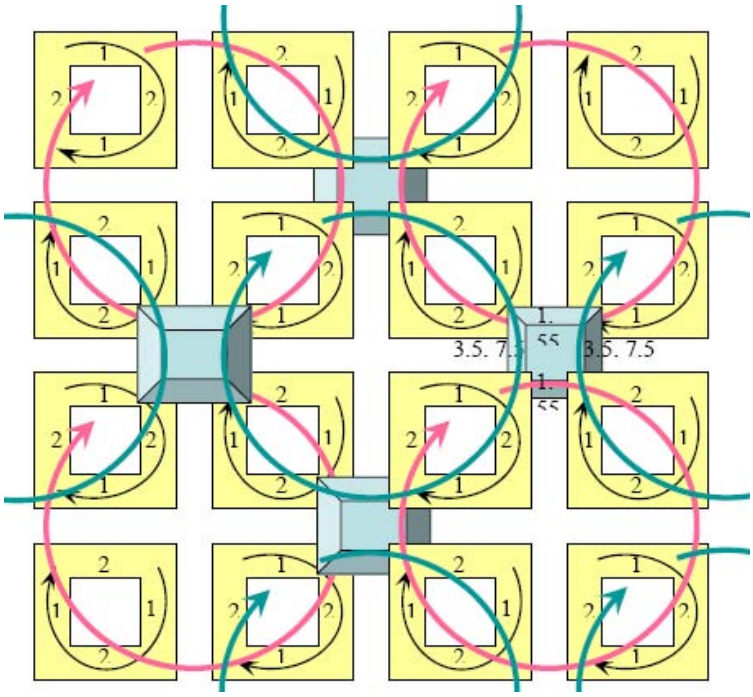

Figure 5.4: Lithographic Patterning Sequence for the envisioned 3-D chiral PBG

Fabricating a complete three-unit-cell thick chiral structure using method A will require eight more X-ray exposures through 2 additional masks. The third mask patterns the resist between adjacent coils. This removes unwanted metallic beams between different alternating coils in the structure in the final pattern. Thus, allowing for the fabrication of the black primary coil in Figure 5.3 while physically isolating the red, purple green and blue-green coils that intertwine the primary coil. This mask is also exposed 15 degrees into the resist at 4 different orthogonal angles as illustrated by the light blue sections in Figure 5.4. Notice that the yellow squares in Figure 5.4 match the small square patterns presented in Figure 5.3 method A. Also note that the direction of rotation is same for all of the structures presented in the design. Furthermore, each adjacent loop is shifted by 90 degrees. This is a direct result of the mask positioning required to complete the structure.

The fourth and final mask pattern shown in Figure 5.5 patterns areas between the chiral structure to prevent development and plating in the dielectric regions of the photonic crystal. This exposure is performed with both mask and substrate perpendicular to the light source. Because the resist is negative, the exposed pattern remains after development preventing metal from plating between any of the individual coils. Risks associated with lithographic patterning of this design lie in the ability to pattern open-loop shifts in the mask and substrate, while maintaining 1 μm alignment.

This is achieved using piezoelectric drive controllers present on the DEX02 X-ray scanner manufactured by Jenoptic Inc. The piezoelectric drive control allows precise open loop displacement up to 50 μm displacement between the mask and substrate. One benefit of using deep X-ray lithography to create the pattern is that the imaged resist will have very little run out through the pattern. In other words, we expect no more than 0.1 μm change in the width of a 1 um line patterned 40 μm into photoresist. Thus we should be able to pattern 1-4 um wide structures precisely within the photoresist allowing for the fabrication of coils nested between one another with gaps of a few tenths of microns.

Also, the chiral crystal itself is then electroplated into the resist mold using any electrodeposited metal (Ag, Au, Ni, Cu, NiCr, NiFe, NiFeCo NiCu, InSb, BiTe, etc.). Release of the photoresist yields a freestanding metal chiral PBG shown in Figure 5.1 made from at any angle orientation required for the design of the band gap. If needed, the structure may then be backfilled with a transparent media to add mechanical support while maintaining the photonic nature of the device. Lithographic patterning of this structure makes the process scalable to a several square inches without significantly increasing patterning time required to generate the

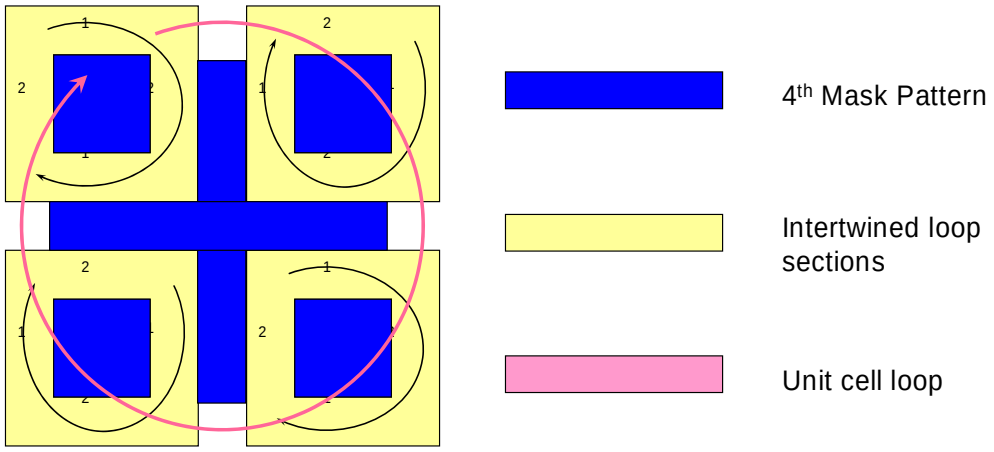

Figure 5.5: 4th mask pattern used to complete DXRL exposure of the 3-D chiral PBG

device. Another benefit to an inherently large area process is the elimination of stitching error present in serial processes [7].

The proposed fabrication scheme can be scaled to generate structures capable of being used in the microwave, THz, and the mid-IR frequency ranges. This allows for a wide range of application spaces including but not limited to tag track and locate operations, dichroic THz spectroscopy, optical filtering, and phase shifters for RF electronics.

Demonstration of the device at frequencies above 10 THz is relatively strait forward. However, IR frequency PBGs will require sub-micron DXRL mask patterns and alignment tolerances as low as 0.25 μm. However experimental validation of sub-micron alignment using a Jenopotic DXRL mask aligner has yet to be demonstrated. One micron alignment has also been demonstrated using this tool for the exposure of 100 um thick mechanical devices.

We propose to use Talbot imaging [9] to create a series of four gratings in a chevron pattern placed on the mask and in planes parallel to the mask should allow a 10X improvement in alignment tolerance—down to ±100 nm. These are gratings are slightly chirped which shows any 2 ambiguities in position in both the *x* and *y* directions. The increased alignment capability provides sufficient resolution reduce the critical dimensions of the device for development of an IR chiral structure. This technique can be easily incorporated using existing hardware.

5.4 Concluding Remarks

Our fabrication scheme will produce a metal structure very similar to two designs proposed in the literature [1,4] but apparently impossible to build. Our lithographic patterning scheme overcomes both the lithographic patterning and geometrical limitations generally presented in the literature allowing for the production a truly unique 3-D chiral band gap material.

Fabrication will be preceded by design optimization using real space based transfer matrix methods coupled with Fourier space plane wave expansion techniques. The complexity of the chiral structure implies large computational data sets. To mitigate this, we propose the introduction of group symmetry based reductions, and genetic algorithm based optimization tools for arriving at optimal device functionality. We expect our structure to have a wide bandgap with very pronounced chiral properties.

The SNL chiral photonic crystal design is similar to (seemingly) unbuildable designs in the literature with full 3D bandgaps. However, the proposed structure is realizable using existing technology and can be built in one inch square tiles that may be arrayed as necessary for large scale applications. Minor variations of these structures can be used in transmission or reflection, and if loaded with quantum dots, could become a circularly polarized IR emitter. These films will enable tag track and locate, dichroic spectroscopy, and optical isolation applications. This work will provide the basis for new, even more complex structures designed for the specific reflection, absorption and transmission of light at certain wavelengths, and polarizations.

5.5 References

[1] O. Toader and S. John, "Proposed Square Spiral Microfabrication Architecture for Large Three-Dimensional Photonic Band Gap Crystals," Science **292** (2001) 1133-1134.

[2] M Thiel *et al.*, "Polarization Stop Bands in Chiral Polymeric Three Dimensional Photonic Crystals," Adv. Mat. **19** (2007) 207-210.

[3] V. Mizeikis *et al.*, "Photonic Crystal Templates Obtained by 2 photon Laser Lithography in SU-8 Photoresist," Mat. Res. Soc. Sym. Proc. **850** (2005) MM4.6.1.

[4] Y. Pang *et al.*, "Chiral Microstructures (Spirals) Fabricated by Holographic Lithography," Optics Express **13**:19 (2005) 7615-7620
[5] S. R. Kennedy, M. O. Jensen, M. J. Brett, "Three Dimensional Square Spiral Photonic Crystal Nanostructures by Glancing Angle Deposition," IEEE ICMENS 2003.
[6] S. R. Kennedy, M. J. Brett, H. Miguez, O. Toader and S. John, "Optical Properties of a Three Dimensional Square Silicon Spiral Photonic Crystal," Photonics and Nanostructures - Fundamentals and Applications **1** (2003) 37-42.
[7] M.O. Jensen and M.J. Brett, " Square Spiral 3D Photonic Bandgap Crystals at Telecommunications Frequencies," Optics Express 12:8 (2005) 1348-1354.
[8] J.D. Williams *et al.*, "Tilted Logpile Photonic Crystals Using the LIGA Technique," Proc. of the SPIE **6249** (2006) 36.
[9] H. Harmam, "Talbot imaging and unification", Appl. Opt., vol. 42, p. 7052 (2003).

6. Publications

1. J.D. Williams, C. Arrington, W. C. Sweatt, D. W. Peters, I. El-Kady, A. R. Ellis, J. Verley, F.B. McCormick, "*Tilted logpile photonic crystals using the LIGA technique*", Proc. SPIE 6289, p. 62890A (2006).
2. Schmidt CF, Sweatt WC**,** El-Kady I, F.B. McCormick, D.W. Peters, S.H. Kravitz, J.C. Verley, U. Krishnamoorthy, D. Ingersoll, W.G. Yelton, G. Subramamia, J.D. Williams, "New Infrared photonic lattice coating", Proc. SPIE 6289, p. 628916 (2006).
3. F. B. McCormick, J. G. Fleming, S. Mani, M. R. Tuck, J. D. Williams, C. L. Arrington, S. H. Kravitz, C. Schmidt, G. Subramania, J. C. Verley, A. R. Ellis, I. El-kady, D. W. Peters, M. Watts, W. C. Sweatt, J. J. Hudgens, "Fabrication and Characterization of Large-Area 3-D Photonic Crystals", 2006 IEEE AEROSPACE CONFERENCE, VOLS 1-9 : 1820-1827, 2006.
4. Rammohan*, R., Farfan*, B.G., Su*, M. F. Reda Taha, M. M., and El-Kady, I. "A Guided Semi-Natural Genetic Optimization for Smart Design of Photonic Crystal Filters", *Engineering Application of Artificial Intelligence*, (Submitted August 2007).
5. Farfan*, B.G., Rammohan*, R., Su*, M. F., El-Kady, I. and Reda Taha, M. M. "Prediction of Photonic Crystals Emitter Efficiency Using An Optimized Fuzzy Learning Approach", *Photonic and Nanostructures – Fundamentals and Applications*, (Submitted August 2007).
6. Sheyka, M.*, Su, M. F.*, Reda Taha, M. M., El-Kady, I. "Sub-micron Damage Identification using Photonic Crystals: Innovative Simulation", *Proceedings of the 6th International Workshop on Structural Health Monitoring*, Stanford, USA, September 2007.
7. Reda Taha, M.M., El-Kady, I. Sheyka*, M. P., Su*, M.F. Khraishi, T., El-Osery A. and Verley J. C. "An integrated simulation environment realizing the ability of nano photonic crystals to detect and quantify submicron and microdamage in materials", *Journal of Computational and Theoretical Nanoscience*, Vol. 4, No. 3, 2007, pp. 494-503.
8. Reda Taha, M.M. "New Sensors for Damage Detection Using Nano Photonic Bandgap Materials", CD Proceedings of the *10th Arab Structural Engineering Conference*, Kuwait, November 2006.
9. El-Kady, I., Reda Taha, M.M. and Su*, M.F. "Application of Photonic Crystals in Submicron Damage Detection and Quantification", *Applied Physics Letters*, Vol. 88, No.26, 253109, June 2006.
10. Verley, J. C., Mani, S.S., Fleming, J. G., El-Kady, I., Khraishi, T. and Reda Taha, M. M. "Experimental demonstration of using nanophotonic crystal sensor systems for submicron damage detection, quantification, and diagnoses", Proc. of SPIE Vol. 6179, 617904, 2006, San Diego, USA.
11. El-Kady, I., Su*, M. F., Reda Taha, M.M., Khraishi, T. and Verley, J.C. "Photonic crystal Sensor Systems for Sub-micron Damage Detection, Quantification, and Diagnoses", *Proc. of SPIE Vol. 6172*, 61720V, 2006, San Diego, USA.
12. Reda Taha, M.M., Sheyka*, M., Su*, M. F., El-Kady, I., Khraishi, T. and Verley, J.C. "An Integrated Numerical Approach for Microdamage Detection Using Nano Photonic Sensors", *Proc. of SPIE Vol. 6179*, 617907, 2006 San Diego, USA.

13. El-Kady, I. and Reda Taha, M.M. "Nano Photonic Sensors for Microdamage Detection: An Exploratory Simulation", *Proceedings of the IEEE Conference on Systems Man and Cybernetics*, Waikoloa, Hawaii, October 2005, pp. 1961-1966.

* Indicates student co-author

7. TA and patent

SD-7948/S-106,222: Uniform Alloy Electroforming of 45/55 Ni/Fe as a Soft magnetic material for High Aspect Ratio MEMS Applications

SD-10003/ S-106,285: Ternary alloy electroplating chemistry for soft magnetic films.
The development of new electroplating processes for very soft magnetic films with very large magnetizations can be directly applied to the production of a novel class of photonic crystals. The development of magneto-optical devices using these materials may have significantly different physical characteristics than similar structures manufactured using non-magnetic materials. Novel materials such as these are being developed under this and other programs.

*SD-7905/S-106,171: Chemically-Robust Hydrophobic Coatings to Minimize Feature Variances in Polymer Electroforming Masks*Swelling of developed PMMA structures patterned using deep X-ray lithography typically produces small deviations in the ideal pattern quality of plated LIGA microstructures. To reduce these errors in the micron and submicron sized features required to produce a "tilted logplie" PBG, Graham and Wheeler have developed a novel method for protecting the PMMA surface from the diffusion on water for short periods of time. This method is currently untested, but can be investigated to improve pattern quality during the 2nd year of this LDRD.

SD-10289/S -109333 Large Area Mask Generation with High Density Nanofeatures
Describes an approach for generation of large area optical and/or imprint mask dense with periodic nanosized features.

SD-10290/S-109334: Direct Laser Imprinting of Large Area Patterned Nanostructures
Introduces a nanopatterning approach based on laser interferometry whereby a periodic array of nanostructures composed of a wide range of materials available in a nanoparticle form that can be directly written on to a substrate.

TA submitted, "Reel-to-reel method for exposing large pieces of photonic bandgap material using deep x-ray lithography"
Looking forward to methods of high-volume production of large-area PBG materials, Sweatt and Williams have formulated a procedure to enable use the LIGA approach in a continuous flow

8. Distribution

MS 1082	James Hudgens	01725
MS 1082	Frederick Mccormick	01727
MS 1082	Ihab El-Kady	01725
MS 1082	David Peters	01727
MS 1082	Ganesh Subramania	01725
MS 1082	John D. Williams	01727
MS 1082	William C. Sweatt	01727
MS 1082	Carrie Schmidt	01723
MS 1082	Stanley Kravitz	01723
MS 1082	Jason Verley	017461
MS 1082	William G. Yelton	01725
MS 9018	Central Technical Files	8944 (electronic copy)
MS 0899	Technical Library	9536 (electronic copy)